High-resolution large-eddy simulation to understand ozone formation and atmospheric oxidation capacity in Houston, Texas

Akinleye Folorunsho[1], Jimy Dudhia[2], John Sullivan[3], Paul Walter[4], James Flynn[5], Travis Griggs[5], Rebecca Sheesley[1], Sascha Usenko[1], Guillaume Gronoff[6], Mark Estes[7], and Yang Li[1]

[1]Department of Environmental Science, Baylor University, Waco, 76798, Texas, USA
[2]National Center for Atmospheric Research, Boulder, 80307, Colorado, USA
[3]NASA Goddard Space Flight Center, Greenbelt, Maryland, USA
[4]Department of Mathematics, St. Edward's University, Austin, Texas, USA
[5]Department of Earth and Atmospheric Sciences, University of Houston, Houston, Texas, USA
[6]NASA Langley Research Center, Hampton, Virginia, USA
[7]Institute of Interdisciplinary Science, St. Edward's University, Austin, Texas, USA

Correspondence to: Yang Li (yang_li3@baylor.edu)

Abstract

Highly reactive volatile organic compounds (HRVOCs) from mobile and petrochemical sources are important players in atmospheric photochemistry that contribute to the formation of ozone (O_3). In a typical elevated O_3 episode, we applied a high-resolution large eddy simulation (LES), coupled with the Weather Research and Forecasting model with chemistry (WRF-LES-Chem) to understand the mechanism of high O_3 production over the Houston area. Our modeling was constrained and evaluated using field measurements from the NASA Tracking Aerosol Convection Interactions ExpeRiment – Air Quality (TRACER-AQ) project, Texas Commission on Environmental Quality (TCEQ), and vertical column density observations from Pandora spectrometers. The modeling results show enhanced performance in the LES domain, compared to the mesoscale models in simulating key chemicals. O_3 sensitivity in the Houston urban area demonstrates a nearly homogenous early morning VOC-limited regime and transits to a noontime NO_X-limited regime. As the day progresses into the afternoon, the atmospheric oxidative capacity (AOC) increases with major contribution from hydroxyl (OH) radical (90 %). High concentrations of alkenes also increased O_3 (8-10 %) contribution to AOC in the late afternoon. The OH reactivity (K_{OH}) is dominated by isoprene (35.76 %), carbon monoxide (CO; 12.98 %), formaldehyde (HCHO; 12.21 %), and alkanes with C > 3 (6.29 %), thus accelerating the production of hydroperoxyl (HO_2) and peroxy (RO_2) radicals. The concentrations of short-lived VOCs such as HCHO and acetaldehyde from the oxidation of HRVOCs, increased in the afternoon, which elevated O_3 production rates under a NO_X-limited regime. The oxidation of isoprene also accelerated the production of HCHO and contributed to the production of HO_2 radicals, thus leading to a high O_3 production rate. This study suggests the possible impacts of NO_X-O_3-VOC sensitivity on O_3 production rates in polluted urban areas with high emission of HRVOCs, and also provides insights on radical chemistry that drives the photochemical processes of O_3 formation. Ultimately, the study underlines the need to control

anthropogenic emissions such as alkenes and HCHO and also highlights the role of naturally emitted isoprene species in elevated urban O_3 levels.

1. Introduction

35   The Houston metropolitan area is home to approximately 7.3 million people and represents a heavily-polluted urban atmosphere due to the presence of complex industrial emissions. Like many polluted urban cities in the United States, Houston is identified as an ozone (O_3) nonattainment area by the U.S. Environmental Protection Agency (US EPA) due to its summertime exceedances of the National Ambient Air Quality Standards (NAAQS) (Shahriar et al., 2015; Botlaguduru et al., 2018), which cause severe human health concerns (Blanchard et al., 2008; Rammah et al., 2020). In 2015, the EPA lowered

40   the 8 h O_3 NAAQS to 70 ppb with projected national attainment by 2025; however, this does not appear realistic over Houston, as evident from the observed O_3 concentrations from the TRacking Aerosol Convection ExpeRiment – Air Quality (TRACER-AQ) 2021 summertime campaign. Generally, O_3 exceedances are highly dependent on the source of primary emissions, chemical reaction rates of primary and secondary oxidants, and meteorological processes (Spiridonov et al., 2019). However, the sensitivity of O_3 to precursors' regimes may also undermine or enhance its production in the atmosphere (Zhou et al., 2014;

45   Ye et al., 2016). Additionally, boundary layer dynamics that affect nonlinear chemistry-turbulence interactions are not well-resolved in mesoscale models with coarse resolutions, yet these processes are essential to understand chemical behaviors in polluted environments (Wang et al., 2023). Thus, this study is aimed to understand the complex pathways of O_3 production and changes in O_3 formation regime in the Houston urban atmosphere using a high-resolution modeling approach.

The O_3 problem in Houston, unlike other large metropolitan cities in the U.S., is a combined product of (i) highly reactive

50   volatile organic compounds (HRVOCs) and nitrogen oxides ($NO_X = NO_2 + NO$) emissions from automobile and industrial sources along the Houston Ship Channel (Souri et al., 2016b; Botlaguduru and Kommalapati, 2020), (ii) variability in the along-shore sea breeze and the planetary boundary layer (PBL) depth (Banta et al., 2011), (iii) the midday reversals of flow patterns or clustering of weak easterly and northeasterly winds (Darby, 2005; Souri et al., 2016a), (iv) potential transport of pollutants from regional and long-range sources (Morris et al., 2006; Berlin et al., 2013), and (v) complex photochemistry

55   under the hot and humid Houston environment (Perring et al., 2013). Because of the heterogeneous automobile emission sources and the presence of multiple oil and natural gas industries in Houston, anthropogenic emissions play an important role in O_3 formation. Primarily, the photochemical processes of ethylene, propylene and 1,3-butadiene from the alkene group are identified as the major anthropogenic VOC contributors to enhanced O_3 formation over Houston (Nam et al., 2006; Kim et al., 2011; Czader and Rappenglück, 2015; Sadeghi et al., 2022). Additionally, the photochemical reactivities of isoprene and

60   monoterpenes from biogenic sources are also major contributors to O_3 formation (Leong et al., 2017; Ma et al., 2022).

The self-cleaning response of the atmosphere to emissions, defined as atmospheric oxidative capacity (AOC), determines the rate of removal of primary pollutants (e.g., CO, NO_X, and VOCs) by oxidizing chemical reactions with O_3, OH, and nitrate radicals (NO_3) (Geyer et al., 2003; Chen et al., 2020). AOC is an important driving force in understanding atmospheric

chemistry, as it determines the removal rate of primary pollutants and the production rate of secondary pollutants (Mao et al.,

65   2010). The total sum of the oxidation rates of these pollutant species is thus used to estimate AOC (Li et al., 2021). Several studies have been carried out to quantify atmospheric oxidation processes and have shown that AOC is dominated by pollutant oxidation from OH radicals, especially in heavily polluted environments (Xue et al., 2016; Li et al., 2018; Zhu et al., 2020). In such environments, the average daytime AOC may range from 6.7×10^7 molecules cm^{-3} s^{-1} to 3.2×10^8 molecules cm^{-3} s^{-1} (Liu et al., 2022). In contrast, NO_3 is insignificant during daytime photochemistry but principally contributes to nighttime AOC

70   (Brown et al., 2011; Chen et al., 2019). However, experimental results from the TexasAQ-2000 campaign suggested that NO_3 contributes significantly to the daytime oxidation of monoterpenes and phenol in Houston (Geyer et al., 2003). Still, there is a very limited understanding of the daytime AOC over the Houston region, as compared to some other major urban polluted regions (Tan et al., 2019; Liu et al., 2022).

O_3 formation is driven by directly emitted precursors, NO_X and VOCs, yet the O_3-NO_X-VOCs photochemistry is nonlinear,

75   and two regimes with different O_3-NO_X-VOC sensitivity have been identified (Sillman et al., 2003). Understanding the photochemical responses of O_3 to reductions in emissions of NO_X and VOCs is crucial to developing an effective O_3 control strategy. In a VOC-limited regime, for example, an incremental increase in VOCs promotes the chemical production of peroxy (RO_2) and hydroperoxy (HO_2) radicals, which increases NO_X cycling and ultimately increases ambient O_3 (Ye et al., 2016). By contrast, in a NO_X-limited regime, increased emissions of NO_X enhance the photolysis of NO_2, thus producing free reactive

80   oxygen atoms, and ultimately reacting with O_2 to produce O_3, resulting in increased O_3 concentrations (Jin and Holloway, 2015). Here, O_3 is produced when the HO_2 and RO_2 radicals convert NO to NO_2 without the consumption of O_3. Previous air quality campaigns over Houston have focused extensively on understanding O_3 photochemistry to NO_X- and VOC-limited regimes. For instance, the TexAQS-2006 campaign (conducted from September to October 2006) showed that the rapid production of O_3 was associated with a VOC-limited regime and a slow production was characterized by a NO_X-limited regime

85   (Zhou et al., 2014). Evidence from the SHARP (April – May 2009) and DISCOVER-AQ (September – October 2013) campaigns also show that O_3 production was more VOC-limited in the morning hours and NOx-limited in the afternoon hours (Ren et al., 2013; Mazzuca et al., 2016). Despite evidence from the TexAQS-2006 campaign that reducing NO_X emissions from power plants led to reduced O_3 concentrations (Cowling et al., 2007; Parrish et al., 2009), high O_3 concentrations up to 120 ppb were observed during the TRACER-AQ campaign. Nevertheless, this sensitivity regime is poorly understood over

90   the Houston region and may be exacerbated by the complex interactions in the region. The exact dependence of O_3 on NO_X- and VOC-limited regimes varies greatly on assumptions and different conditions, hence, threshold criteria for transition regimes are likely to change depending on changes in emission rates and patterns (Zhang et al., 2023), which may create a shift in O_3 regimes. Thus, we need an accurate modeling interpretation of chemical and physical processes to more accurately determine O_3-NO_X-VOCs sensitivity.

95   Since O_3-NO_X-VOCs sensitivity is mostly determined from photochemical air quality models (Sillman et al., 2003; Song et al., 2010; Li et al., 2011; Goldberg et al., 2016; Du et al., 2022), accurate modeling representations of chemical and physical processes are crucial to better determine O_3 formation regime, thus more effectively supporting ozone mitigation strategies in

Houston. However, previous model-based studies are subject to large uncertainties from simulated O_3 concentration and its precursors. The diurnal evolution of the PBL can significantly influence the mixing, transport, and chemistry of pollutants (Miao et al., 2019; Xiang et al., 2019), and thus must be accurately resolved in modeling. Based on previous studies, turbulence results in reductions of chemical reaction rates in the boundary layer, as a result of negatively correlated concentrations and vertical velocities (Li et al., 2016). Stockwell (1995) showed turbulence causes a non-uniform mixing of gas-phase trace species, thus limiting the accuracy of chemical models. This is particularly true if the model resolution is too coarse to resolve heterogeneous urban emissions and wind flows (Chen et al., 2009; Uebel and Bott, 2018). Also, these chemical models cannot adequately resolve the concentration and transport of O_3 pollutants in convective, unstable atmospheres due to a misrepresentation of boundary layer evolution (Li et al., 2016; Cuchiara et al., 2014). In a recent study, Wang et al. (2023) showed an improved modeling-observation agreement of the spatial and vertical distributions of key chemical species (e.g., O_3, NO and NO_2) from large eddy simulation (LES) compared with mesoscale simulations, indicating LES is an effective tool to resolve turbulence effects on chemical reactions. WRF-LES-Chem is advantageous due to its potential to improve the physical and chemical processes of pollutants at different scales.

In this work, we perform high-resolution simulations using WRF-LES-Chem over an O_3 exceedance period in September 2021 during the TRACER-AQ experiment, aiming to provide a comprehensive understanding of photochemical and physical processes involved in O_3 formation over Houston. Recent modeling studies have investigated ozone episodes during the TRACER-AQ campaign (Soleimanian et al., 2023; Li et al., 2023; Liu et al., 2023). This work expands upon those efforts by applying higher resolution LES simulations on the particular case day of September 8, 2021. Model results are comprehensively validated utilizing long-term ground-based observations from the TCEQ monitoring stations, measurements from the TRACER-AQ campaign, and observations from ground-based Pandora spectrometers to ensure modeling accuracy. This study also assesses spatial and temporal variability of the O_3 formation regime and investigates AOC, which can provide useful information to environmental managers to better control O_3 pollution over Houston.

2. Methodology

2.1 Model description and set-up

2.1.1 Dynamic settings

We use the WRF-Chem model (Grell et al., 2005; Fast et al., 2006) version 4.4 with the integrated rate reactions capability that allows for the investigation of specific chemical pathways. Since LES is better suited to represent the PBL evolution and the transport of large eddies, we use a WRF-LES-Chem approach to simulate the concentration and transport of O_3 pollutants in convective, unstable atmospheres evolution (Li et al., 2016; Wang et al., 2023). Our modeling consists of four domains (D01 – D04) with horizontal grid resolutions of 8.1 km, 2.7 km, 900 m, and 300 m from outermost to innermost domains on a Lambert conformal projection (Fig. 1). The first three domains (D01 – D03) represent mesoscale setups while the innermost

domain (D04) is the LES domain. While the ideal LES resolution may range from 100 m and below, we select a 300 m

130 resolution due to the computational feasibility of our study that aims to better account for both boundary layer dynamics and detailed atmospheric chemistry, as used in other literature (e.g., Wang et al., 2023). At this resolution, we aim to reach a compromise between model computational efficiency and model resolution, since LES at finer scale resolutions are otherwise too computationally expensive, especially given the size of our innermost domain that aims to focus on most of the Houston area. The LES domain extends over the Houston urban area, including all TRACER-AQ measurement stations and Houston

135 Ship Channel, and includes 427 x 415 grid cells horizontally. A two-way nesting approach (the inner domain provides feedback to the outer domain) is set up between the domains. We perform two simulations where a two-way nesting between domains D01 and D02 is used to drive another two-way nested simulation between domains D03 and D04. The simulations are performed at a time step integration of 24 seconds and 1.8 seconds, respectively. The vertical layers comprise of 61 levels across all domains with the lowest layer within ~20 m near the surface, and include 25 layers located within the PBL to resolve

140 boundary layer processes (~1.5 km). The vertical grid spacing gradually increases up to the top of the model at 50 hPa.
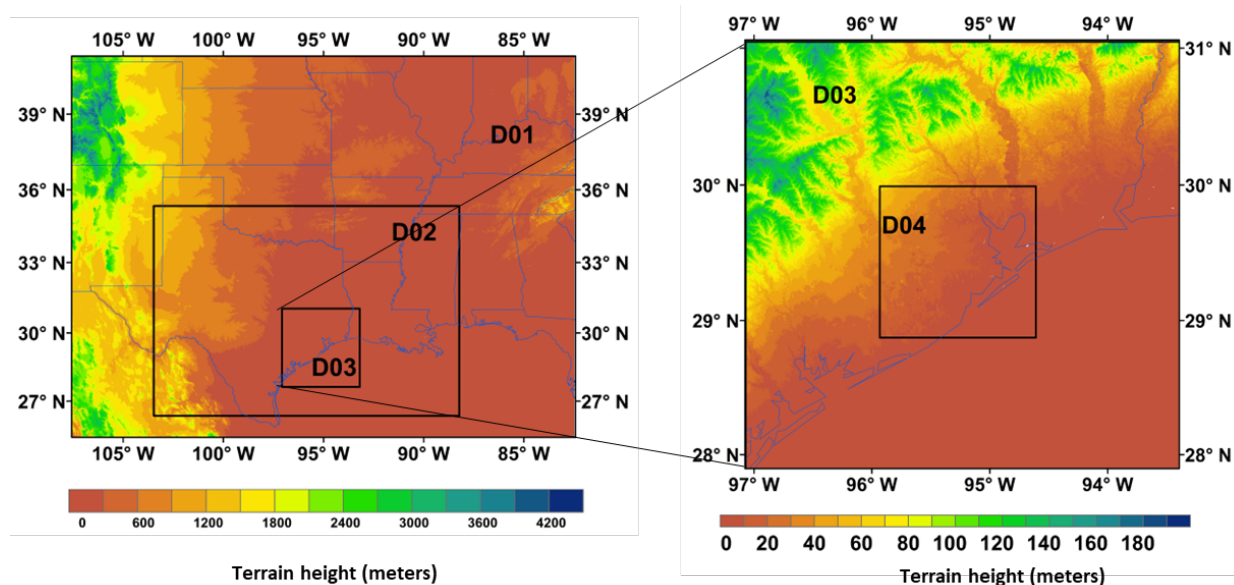
Figure 1: The four-layer domain setup with the background contour showing average topography.

To better examine chemical processes in a complex, dynamic urban atmosphere like Houston, a more accurate meteorological

145 product is needed to drive the simulations. We therefore examine model sensitivity to meteorological initial and boundary (IC & BC) conditions from the High-Resolution Rapid Refresh (HRRR; Dowell et al., 2022) and the Final Operational Global Analysis (NCEP-FNL; NCEP, 2000) data, with these two meteorological products widely used in previous studies (Jiménez et al., 2022; Pinto et al., 2021; Gholami et al., 2021) (Fig. S1). NCEP-FNL has a spatial resolution of 1° x 1° and is provided at a 6 h interval. HRRR is provided at a horizontal grid spacing of 3 km and available every 1 h up to 48 h forecasts. We

150 perform a two-way nested simulation using domains D01 and D02 without chemistry to test the performance of both FNL and

HRRR as IC & BC. The simulation extends from September 6, 2021 (00:00 UTC; September 5, 19:00 CDT) to September 9, 2021 (00:00 UTC, September 8, 19:00 CDT). Our model results, driven by the two datasets show similar spatial distributions of the surface heat budget (Fig. S1). We also show a wind rose diagram which gives a succinct view of how wind speed and direction are typically distributed at a particular location. Here, a prevailing north-westerly wind based on the TCEQ in-situ observations is observed. The model results driven by the NCEP-FNL more closely matches the TCEQ observed north-westerly wind than HRRR.. Wind fields are key parameters to determine the transport and mixing of pollutants. Hence, although HRRR has a much higher spatial resolution, we select the NCEP-FNL meteorological product to provide a more realistic dynamic field in our simulations.

Key physical parameterizations in our modeling include: the Rapid Radiative Transfer Model for GCMs (RRTMG) scheme for longwave and shortwave radiation (Iacono et al., 2008), Morrison double moment scheme for cloud microphysics (Morrison et al., 2009), the Noah land surface model (Chen and Dudhia, 2001), and the revised MM5 Monin-Obukhov for the surface layer scheme (Jiménez et al., 2012). The Grell 3D scheme (Grell and Dévényi, 2002) is used for cumulus parameterization to resolve sub-grid cloud processes for coarser resolution (D01 and D02), while it is turned off for D03 and the LES (D04) domain. We use the Yonsei University PBL scheme (YSU; Hong et al., 2006) to parameterize the sub-grid scale turbulent fluxes within the PBL for the mesoscale domains. YSU represents a non-local and first-order closure scheme to estimate turbulent diffusion, where vertical diffusion is expressed as a function of a non-local gradient adjustment term. This PBL option is turned off for the LES domain to resolve large eddies directly, however, finer-scale eddies are resolved by the three-dimensional 1.5 order turbulent kinetic energy (TKE) closure (Deardorff, 1970).

Simulations for the mesoscale domains (D01 – D02) cover the period from September 6, 2021 (00:00 UTC) to September 9, 2021 (00:00 UTC), which corresponds to Houston's local time from September 5, 2021 (19:00 Central Daylight Time, CDT) to September 8, 2021 (19:00 CDT), with the first 20 hours as the spin-up time. The output was used to drive parallel simulations for D03 and the LES domain and cover the period from 11:00 to 21:00 UTC (06:00 – 16:00 CDT) on September 8, 2021.

2.1.2 Chemistry settings

Our study adopts the recent MOZART (Model of Ozone and Related Chemical Tracers) tropospheric chemistry scheme (T1; Emmons et al., 2020) to represent the gas-phase chemistry. MOZART-T1 is a more comprehensive chemistry scheme compared with previous versions. It includes 151 gas-phase chemical species, 65 photolysis reactions and 287 kinetic reactions. Compared to previous versions of the MOZART scheme, specific modifications are made to the oxidation of isoprene and terpenes in MOZART-T1, as well as the speciation of aromatic and organic nitrate to improve the representation of O_3 and secondary organic aerosol (SOA) precursors (Emmons et al., 2020). The Tropospheric Ultraviolet-Visible (TUV; Tie et al., 2003) transfer scheme is used for the estimation of photolysis rates. We also use output from the Community Earth System Model - Whole Atmosphere Community Climate Model (CESM2-WACCM; Liang et al., 2022; Gettelman et al., 2019) as the IC and BC of chemical species in our simulations. Initial conditions and boundary conditions for each nested domain are generated from the parent domains, which are produced by the 8.1 km simulation. The Model of Emissions of Gases and

Aerosols from Nature (MEGAN; Guenther et al., 2006) and the 2017 US EPA National Emissions Inventory (NEI; Reff et al., 2020) are used as biogenic and anthropogenic emissions, respectively, while the recent release of the Fire Inventory from NCAR (FINNv2.5; Wiedinmyer and Emmons, 2022) is used to provide fire emissions and biomass burning. NEI emissions data consists of point and non-point sources at a 12-km resolution and are downscaled to respective model resolutions for inner domains through WRF nesting. Emissions from MEGAN and FINN are available at a base resolution of 1 km, and all emission inventories are mapped to the same resolution for each of the domains. Our simulation results with the 2017 NEI show overestimated NO_X concentrations, as found in previous urban studies (Choi and Souri, 2015; Souri et al., 2016a; Silvern et al., 2019; Herrmann and Gutheil, 2022). To more accurately represent emissions during the high ozone episode in Houston, we compare simulated concentrations of NO and NO_2 with their observations from TRACER-AQ and develop scaling factors of 0.3 and 0.2, respectively, to adjust NEI emissions of NO and NO_2. The total NO_2 emission over Houston accounts for 11.32 % of the total emitted NO_X based on the NEI over the study period. On average, the diurnal pattern of the rescaled NO_X emission is characterized by high early morning emissions at ~0.65 mol km^{-2} h^{-1} and then peaks in the late afternoon at ~0.74 mol km^{-2} h^{-1}. The results we show in this study are based on simulations with the scaled NO_X emissions. While existing studies show large uncertainties in previous versions of FINN which may result from the coarse resolution of the active fire product (Faulstich et al., 2022; Liu et al., 2020), the improved spatial resolution of the VIRS product in the FINNv2.5 provides more sensitive detection of fires at local and regional scales to minimize the estimated emission uncertainties (Wiedinmyer et al., 2023).

2.2 Observational data

2.2.1 TRACER-AQ airborne observations

The NASA TRACER-AQ experiment aimed to provide a robust understanding of how pollutants vary spatially, vertically and temporally over the Houston region. A wide range of instruments were operated during TRACER-AQ, which generated large measurement datasets from airborne, ship-based, mobile and stationary ground platforms (Knapp and Boyer, 2022; Griggs et al., 2024). Continuous atmospheric profile measurements from Sondes and Lidar provide unique and valuable data to understand the variability of pollutant profile and column concentrations (Gronoff et al., 2019). We use measured vertical distributions of temperature, relative humidity, wind speed, potential temperature, and ozone from field ozonesondes, which were launched from Galveston Bay and La Porte stations (see Fig. 2) on 8 September 2021 at 12.47 CDT and 13:07 CDT, respectively. Since the balloon drifts during its ascent in response to background winds, we use the nearest model grids along the sounding trajectory for accurate comparison.

2.2.2 TCEQ and Pandora ground station measurements

In-situ measurements from 18 Texas Commission on Environmental Quality (TCEQ) stations are used to evaluate our simulated surface meteorological fields (temperature, wind speed, vertical velocity and water vapor) and pollutant (O_3, NO_2)

215 concentrations. Data from 67 stations in Houston are available in the TCEQ Texas Air Monitoring Information System (TAMIS) database at every hour. Data coverage from TCEQ stations is widely used in previous studies for VOCs, hydrocarbon and meteorology monitoring (Schade and Roest, 2018; Vizuete et al., 2022).

We also use level 2 (L2) data products retrieved from the two Pandora spectrometers in La Porte (29.67° N; 95.06° W) and the University of Houston (UH; 29.72° N; 95.34° W), including column concentrations of O_3 as well as surface concentrations of

220 HCHO and NO_2 (Fig. 2). Pandora spectrometers directly use the differential optical absorption spectroscopy (DOAS) method to obtain slant column density from measured solar irradiances, and translated to estimate the tropospheric column of pollutant variables (Platt and Stutz, 2008; Herman et al., 2009, 2018; Thompson et al., 2019). Since light detected by Pandora spectrometer systems can transverse through different paths depending on the observation geometry, it allows the detection of trace gas absorption at various altitudes. Previous studies found good agreements between Pandora measurements and

225 calibrated in-situ measurements as well as between Pandora and satellite retrieved data products (Baek et al., 2017; Martins et al., 2016; Thompson et al., 2019; Spinei et al., 2018). The sky-scanning properties of the Pandora spectrometer are critically sensitive to trace gases absorptions in the lower atmosphere and can be used to measure the tropospheric column of NO_2 and HCHO (~4 km top of atmosphere; TOA), while measurements at large zenith direction provide information on O_3 stratospheric gas absorption properties.
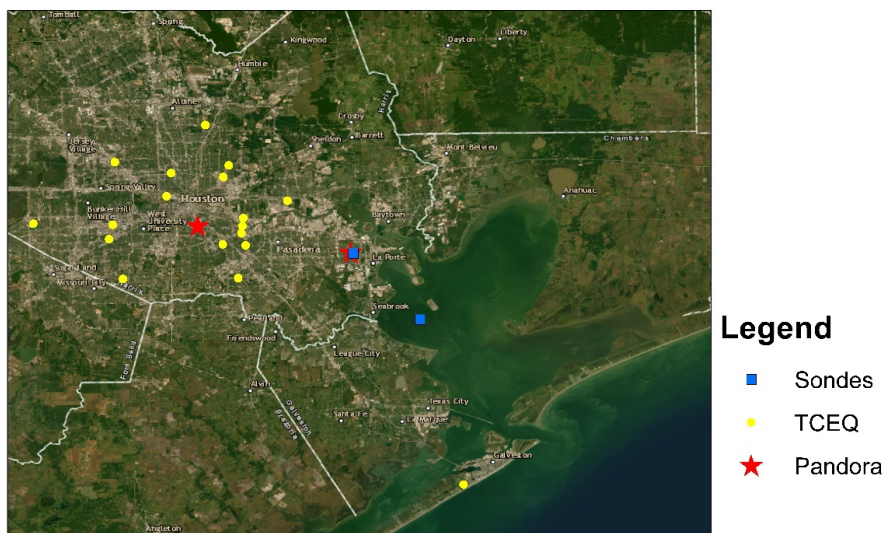
230

Figure 2: Locations of the TCEQ monitoring stations, TRACER-AQ sondes and Pandora spectrometers in the Houston region (Credits for the background image: Esri, HERE, Garmin, © OpenStreetMap contributors, and the GIS user community).

2.3 O_3 production rate and sensitivity regime

In daytime photochemical reactivity, the O_3 production rate (PO_3) is primarily dependent on NO_2 production from the reactivity

235 of NO with RO_2 and HO_2 radicals. In contrast, the loss of O_3 depends on the photolysis of O_3, the formation of nitrate acid from OH and NO_2, and the ozonolysis of alkenes. Overall, we estimate net PO_3 using Eq. 1 as defined by Mazzuca et al. (2016).

$$
\begin{aligned}
\boldsymbol{Net\ P(O_3)} = {}& k_{HO_2+NO}[HO_2][NO] + \sum k_{RO_{2i}+NO}[RO_{2i}][NO] \\
& - k_{OH+NO_2}[OH][NO_2][M] - P(RONO_2) - k_{HO_2+O_3}[HO_2][O_3] \\
& - k_{OH+O_3}[OH][O_3] - k_{O(1D)+H_2O}[O(1D)][H_2O] - L(O_3 + alkenes)
\end{aligned} \tag{1}
$$

240

Here, the k terms represent the reaction rate coefficients; RO_{2i} is the individual organic peroxy radicals. Several indicators are used to determine the response of O_3 production to NO_X and VOC emissions, thus to determine NO_X-limited and VOC-limited regimes for O_3 formation. More predominantly used methods include the ratio of the rate of radical loss via NO_X reaction (L_N) to the total primary radical production (Q) (Mazzuca et al., 2016; Zhou et al., 2014; Yu et al., 2020; Zhang et al., 2023) and

245 HCHO to NO_2 ratio (FNR; Duncan et al., 2010; Jin and Holloway, 2015; Schroeder et al., 2017; Goldberg et al., 2022; Chen et al., 2023). As proposed by Kleinman (2005), L_N/Q can be calculated by dividing the rate of radical loss via NOx reaction (L_N = R4 + R5 + R6a – R6b) by the total of primary radical productions (Q = 2*R1 + 2*R2 + R3). The photodissociation of O_3 and HCHO represent the primary pathways for the production of HO_X (HO_2 + OH) radicals (R1-R3), while radical termination through NO_X is summarized in R4-R6. A reactivity-weighted threshold of 0.5 indicates the transition between a

250 VOC-limited regime and a NOx-limited regime, with L_N/Q < 0.5 representing a NO_X-limited regime, while L_N/Q > 0.5 indicating a VOC-limited regime (Kleinman et al., 2001; Kleinman, 2005).

Radical Initiation:

$$O_3 + hv \rightarrow O^1D \qquad\qquad\qquad \text{R1}$$
$$O^1D + H_2O \rightarrow 2OH$$
255 $$HCHO + hv \xrightarrow{O_2} 2HO_2 + CO \qquad \text{R2}$$
$$Alkene + O_3 \rightarrow RO_2 \qquad\qquad\quad \text{R3}$$

Radical loss via NOx:

$$OH + NO2 \rightarrow HNO_3 \qquad\qquad \text{R4}$$
260 $$RO_2 + NO \rightarrow Orgaic\ nitrate \quad\ \text{R5}$$
$$CH_3CO_3 + NO_2 \rightarrow PAN \qquad\ \text{R6a}$$
$$PAN \rightarrow CH_3CO_3 + NO_2 \qquad \text{R6b}$$
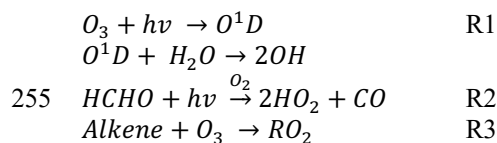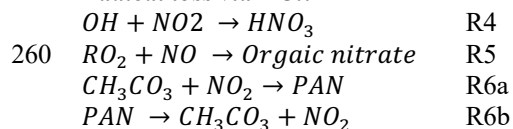
Research on FNR as an indicator for PO3 uses HCHO as an estimate of the oxidation of short-lived VOC emissions (Duncan

265 et al., 2010). In their study, HCHO and NO_2 are retrieved from satellite instruments; hence this ratio is introduced as a non-local or regional proxy for the chemical regime (Duncan et al., 2010). Previous studies have adopted varying FNR threshold values to indicate NO_X or VOC-limited regimes in regions with distinct emission characteristics (Wang et al., 2021; Chen et al., 2023). In a heavily polluted environment from HRVOC emissions, the assumption of HCHO as a proxy for short-lived VOCs may not hold, thus affecting the FNR threshold (Schroeder et al., 2017; Souri et al., 2020). For example, when a large

270 influx of HRVOC emissions is introduced in a heavily polluted atmosphere, radical species and NO_X partitioning reach new steady state concentrations faster while HCHO may be slower to respond, which temporarily reduces the ability of HCHO to act as a proxy until it reaches a new steady state (Schroeder et al., 2017). Tonnesen and Dennis (2000) used a threshold of 1.0 to estimate the transition of the two regimes over the New York area. Duncan et al. (2010) assumed a VOC-limited regime when FNR < 1.0 and a NO_X-limited when FNR > 2.0, which are also adopted in other studies (Tang et al., 2012; Jin and

275 Holloway, 2015; Chen et al., 2023). There is still a high uncertainty relating to the transition threshold between the two regimes for FNR, and peak values of FNR may reach up to ~6 in southeastern US cities (Li et al., 2022). Hence, we apply both the FNR and L_N/Q methods to examine O_3 formation regimes and use the L_N/Q to investigate the FNR transition threshold in the Houston area. Calculations are conducted using model results.

2.4. Model evaluation metrics

280 To quantitatively evaluate the reliability of the model, we calculate the mean absolute error (MAE) and root mean square error (RMSE) for the comparison of modeled results with TCEQ observations. All comparisons are made on time-paired data for air temperature, wind speed, O_3 and NO_2 across selected stations. MAE and RMSE are calculated using the following equations:

$$MAE = \frac{\sum_{i=1}^{n} |y_i - x_i|}{n} \tag{2}$$

285 $$RMSE = \sqrt{\frac{\sum_{1=1}^{n} (y_i - x_i)^2}{n}} \tag{3}$$

where y_i and x_i are time-paired model and TCEQ observation values.

3. Results

3.1 Spatial distributions

Since local production of O_3 is also influenced by temperature and water vapor (Kleinman, 2005; Duncan et al., 2010), it is 290 important to capture the accurate representation of the meteorology. Thus, we first investigate horizontal distributions of simulated key meteorological fields, including temperature, horizontal and vertical wind speed, and water vapor mixing ratio near the surface across in model domains D02 and D04 on September 8, 2021. As we apply an online two-way coupling that allows feedback between the intermediate domain D03 and the LES domain D04, results from the mesoscale D03 are modified by feedback from the LES thus these two domains show similar spatial characteristics. D03 results are therefore not shown 295 nor further discussed. Two time slices, including 09:00 CDT (Fig. S2) and 15:00 CDT (Fig. 3), are selected to represent distinct convective hours. Here, meteorological conditions reveal that warm, moist air prevails in the broad Houston region during the morning, while hot, drier air with prevailing northerly winds dominate the inland Houston during the afternoon. From 09:00 CDT to 15:00 CDT, increasing solar radiation drives a more dynamic boundary layer, with temperature, wind speed and water vapor mixing ratio all demonstrating more heterogeneities in the afternoon. We therefore show maps of the meteorological 300 fields at 15:00 CDT here but keep the 09:00 CDT fields in the Supplementary Materials as a reference. At both times, model generally overestimates (underestimates) temperature (horizontal wind speed), although the results from the LES domain show better agreements with observations from the TCEQ stations than the results from the mesoscale D02 simulation, especially at 15:00 CDT under a more developed PBL condition. The post-sunrise (9:00 CDT) surface temperatures are relatively low and

exhibit homogeneous distributions both inland and over the sea. As the day progresses into the afternoon, surface temperature

305   rises over land due to increased solar radiation, with higher temperatures dominating the Central Houston region due to the

impact of the urban heat island (Marsha et al., 2018). Vertical wind speed also indicates enhanced daytime convective updrafts

at the surface in the LES domain compared to the mesoscale domains. In addition, both the mesoscale and LES results show

warmer biases compared to observations, though the LES domain D04 has lower RMSE of 2.39 °C and 2.74 °C for temperature

at the Deer Park and Clinton stations compared to 2.57 °C and 3.53 °C from the mesoscale domain D02 (Table S1). Similarly,

310   compared with the observed average wind speed of 4.67 m s^{-1}, MAE values show a lower model bias for the LES at 2.42 m s^{-1} than 2.91 m s^{-1} for the mesoscale domain at the Clinton station. While turbulence may be better resolved at finer LES

resolutions (Wang et al., 2023), our LES results with a horizontal spacing of 300 m demonstrate reasonable capacity to resolve

PBL dynamics as in Lebo and Morrison (2015) and Grant et al. (2022).
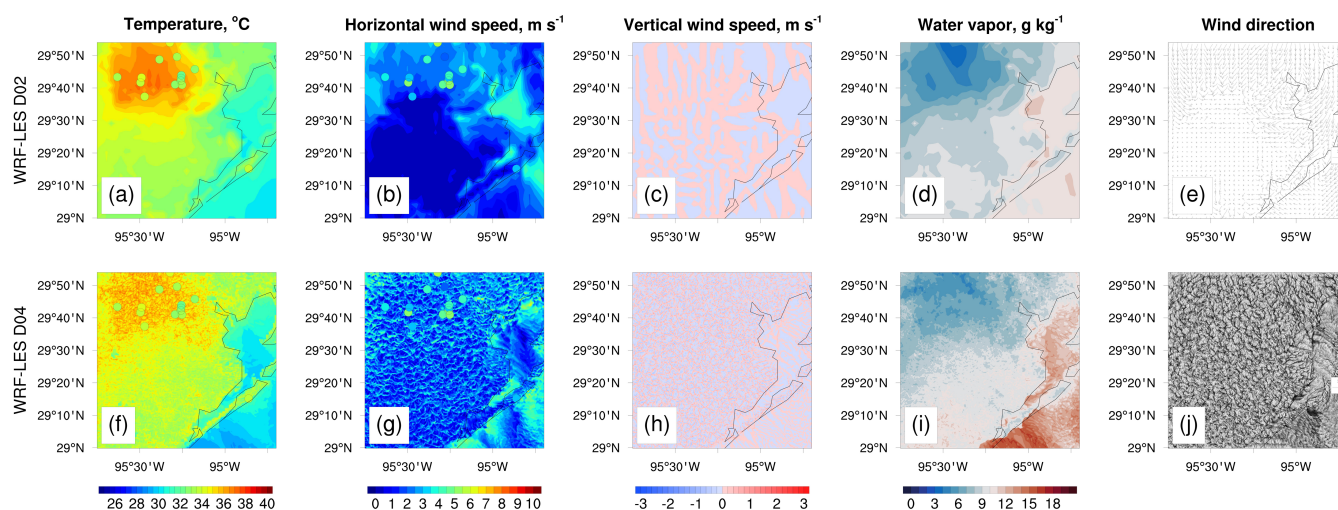
315

Figure 3: Contour maps are horizontal distributions of simulated temperature (first column), horizontal wind speed (second column), vertical wind speed (third column), water vapor (fourth column), and wind direction (fifth column) near the surface at 15:00 CDT for D02 (first row) and D04 (second row) simulations. Circled dots represent measurements from TCEQ stations.

320   The near-surface concentrations of modeled O$_3$, NO$_2$, HCHO and isoprene during the afternoon (15:00 CDT) are shown in

Fig. 4. Overall, the model shows slight overestimation of simulated O$_3$, NO$_2$, and HCHO. However, the model captures well

the diurnal variations of these chemical species when compared with observations. In contrast to the LES domain D04, the

mesoscale domain D02 shows minimal spatial variation due to its coarse resolution. Like O$_3$, the LES domain D04 shows

improved model resolving capacity for chemical species as they show the best agreement with observations in the morning

325   and afternoon hours. Peak O$_3$ concentrations occur around 15:00 CDT. While the LES domain (D04) slightly overestimates

observations of O_3 over Galveston Island by up to 10 ppb, our model results in D04 still demonstrate good agreement with observations from the majority of the TCEQ stations, particularly in the Central Houston region with a dense observation network. High NO_2 concentrations are both observed and simulated in the morning hours (Fig. S3), with a maximum surface concentration of 42 ppbv identified in Central Houston, resulting from road traffic emissions during rush hour (Souri et al.,

330   2016b). In the late afternoon, the photolysis of NO_2 is enhanced, thus resulting in reduced NO_2 concentrations. Overall, the model captures NO_2 dominant zones within the Central Houston and the Houston Ship Channel areas, as their presence in the atmosphere is largely dependent on anthropogenic emissions. The statistical comparison of both the mesoscale and LES domains with TCEQ observations (Table S1) show an overestimation of O_3 mixing ratio, though LES simulates a lower bias (RMSE = 5.49 ppbv, MAE = 4.32 ppbv) compared to the mesoscale domain D02 (RMSE = 16.01 ppbv, MAE = 15.05 ppbv)

335   at the Deer Park station. Like O_3, the LES results exhibit lower biases at both stations for NO_2 when compared with the TCEQ observations. Although the LES performs better, the results in this domain still show biases, which are likely induced by the uncertainties and coarser resolutions of the emissions inventories used in this study (Herrmann and Gutheil, 2022). Also, the temporal variability of the WACCM boundary conditions used in our simulations may introduce transport errors as identified in other regional modeling studies (Tang et al., 2023). In contrast to NO_2, HCHO follows an opposite diurnal pattern with

340   lower concentration in the morning hours and higher concentration in the afternoon due to photochemical reactions of primary and oxygenated VOCs (Zhang et al., 2022). The temporal distributions of NO_2 and HCHO are different as afternoon HCHO is a product of emitted HCHO and secondary HCHO produced from other precursors, thus higher in the afternoon when atmospheric oxidation is high (Nowlan et al., 2018). Isoprene, a major precursor to daytime O_3 production, shows higher concentrations in the late afternoon (Fig. 4), as the biogenic emissions are dependent on temperature and light (Rinne et al.,

345   2002; Guenther et al., 2006; Zeng et al., 2023). In addition, surface and column concentrations of NO_2, HCHO and O_3 from Pandora spectrometers are used to evaluate the model's performance as shown in the Supplementary Materials (Fig. S4). We also see the LES domain D04 show improved column concentration of HCHO, NO_2 and O_3, which is consistent with the diurnal variations of the pollutants from the Pandora spectrometers.
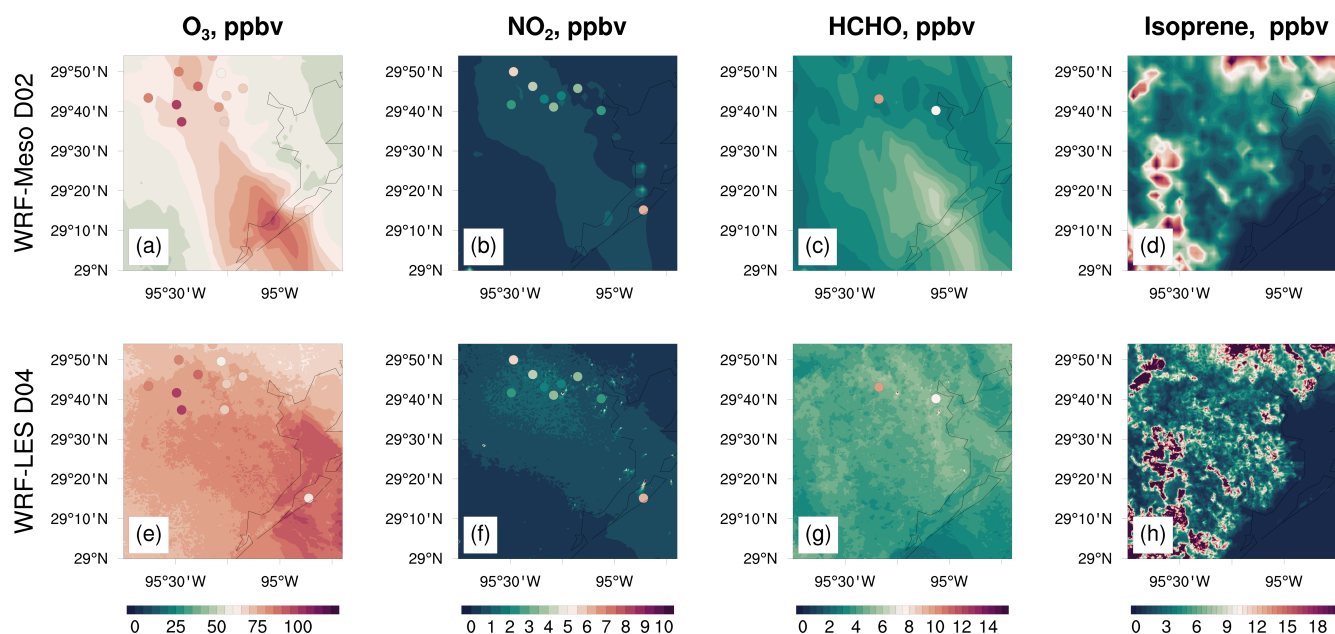
350

Figure 4: Contour maps are horizontal distributions of simulated O₃ (first column), NO₂ (second column), HCHO (third column) and isoprene (fourth column) near the surface at 15:00 CDT for D02 (first row) and D04 (second row) simulations. Dots represent TCEQ observations of O₃ and NO₂ and Pandora observations of NO₂ and HCHO. Isoprene and other key VOCs are validated separately.

To understand O₃ formation, an accurate model interpretation of its VOC precursors is needed. We, therefore, validate our

355 modeled VOCs by comparing key VOCs that are measured by the Proton Transfer Reaction – Mass Spectrometry (PTR-MS) at San Jacinto Battleground State Historical site (29.753 °N, 95.091 °W), a TRACER-AQ site (Fig. 5). The comparison results indicate the model adequately reproduces observations, with results from the LES domain D04 better matching observed VOCs, especially for acetaldehyde, isoprene, HCHO, methyl ethyl ketone (MEK), toluene and xylenes. Although acetone is largely underestimated in the mesoscale D02 simulations, the LES results better reproduce observations. We also acknowledge

360 that the difference in measurement time (30 s) and model average time (1 h), as well as representing a station with one model grid cell may account for further disparities between the model and station measurement. This intercomparison considers daytime VOC concentrations, while the San Jacinto site has previously reported anomalous, high isoprene and MEK concentrations overnight that may likely arise from anthropogenic activity instead of biogenic emission and oxidation (Shrestha et al., 2023). The daytime intercomparison here likely reflects the local biogenic contributions to isoprene.

365
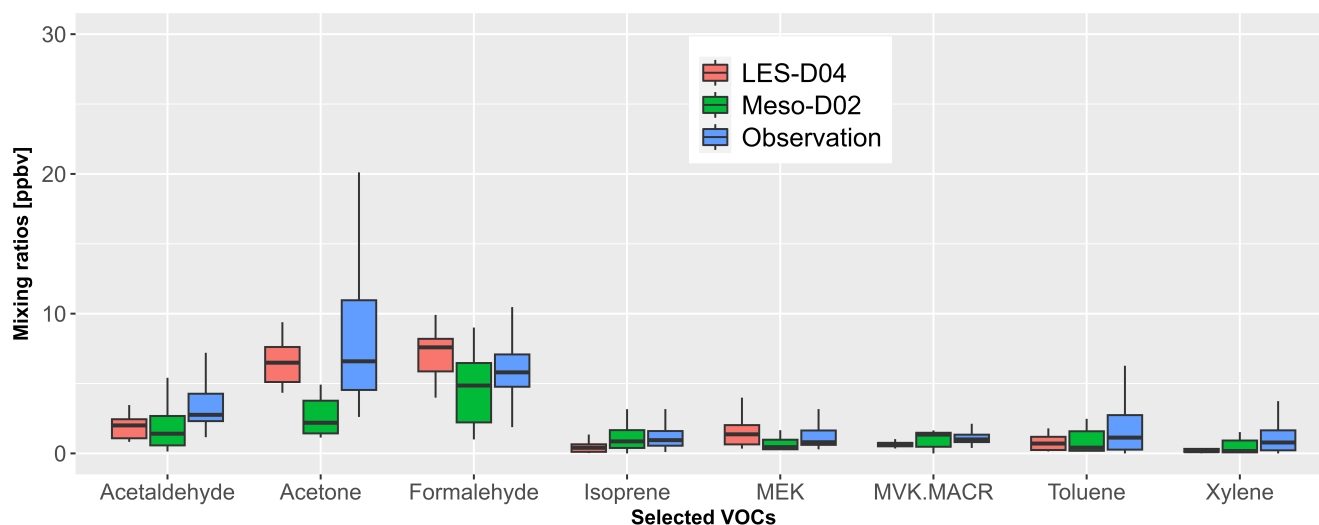
Figure 5: Comparison of daily concentration averages (over 8:00 – 16:00 CDT) of selected VOCs from our simulations in D02 and D04 and measurements at the San Jacinto Battleground State Historical site.

3.2 Vertical Profiles

We next examine simulated vertical profiles of key meteorological and chemical fields to study the role of boundary layer mixing in modifying surface levels of air pollutants. Simulated vertical profiles of O_3 and key meteorological variables are compared with sonde measurements from TRACER-AQ over two launch sites, La Porte and Galveston Bay, as shown in Fig. 6. The trajectories of sondes can drift gradually from the launch sites to higher altitudes; therefore, simulation results aloft are selected according to sonde positions to minimize comparison bias of the vertical profiles. For potential temperature, the LES domain D04 provides a better match with observations than the mesoscale domain D02. Additionally, the LES domain D04 simulates a PBL height (PBLH) of approximately 1.3 km at the Galveston Bay launch site, comparable with sonde measurements of about 1.1 km (Fig. 6d). At the Galveston Bay site, the LES overestimates wind speed by ~3 m s^{-1} near the surface and ~2 m s^{-1} at 1.3 km altitude when compared to sonde observations. Similarly, from the surface to ~0.5 km altitude, wind speed is also overestimated by the model by a maximum value of ~1.5 m s^{-1}, a 30 % difference based on the observations at the La Porte site. For relative humidity, the model simulates contrasting patterns below and above ~1.3 km altitude and underestimates relative humidity by 30 % below this transition altitude in the Galveston Bay region. Compared with the Galveston site, modeled vertical profiles of relative humidity depict smaller biases compared to observations at the La Porte site, with less bias from the LES domain than the mesoscale domain. The larger model-observation discrepancy at the Galveston station may be related to the proximity of the station to the open water surface of the Gulf of Mexico, as the rapid changes in air dynamics over the land-sea interface typically could not be accurately resolved through modeling (Ward et al., 2020). In addition, land surface parameterization in models in accurately modifying surface sensible and latent heat fluxes may vary over land and near water surfaces, thus further affecting simulated moisture metrics (Kantha Rao and Rakesh, 2019). Similarly, the NCEP-FNL meteorology at a 1° x 1° coarse resolution used to drive our modeling may also introduce simulated

moisture bias at upper altitudes, which could primarily be due to inaccurate surface soil moisture that cannot be well represented at this coarse resolution (Ochsner et al., 2013).

The vertical structures of temperature show reasonable performance compared with observations at both sites, with the LES domain slightly performing better (+0.5 °C bias) than the mesoscale domain (+0.7 °C bias). Simulated O_3 profiles also show biases comparing with observed profiles. The LES domain D04 overestimates O_3 mixing ratio while the mesoscale domain

395 D02 underestimates it over both sites. Discrepancies between model and observations may be attributed to the time lag between sonde measurements and simulation outputs. Minute-to-minute changes in wind speed and directions affect the distribution and dispersion of air masses (Li et al., 2019), thus the time differences may affect the model-observation comparison. In addition, the accuracy of reanalysis meteorological datasets, which are used to drive model simulations, in representing vertical profiles of key meteorological factors and their diurnal evolution may also contribute to the comparison discrepancy. We

400 further investigate the temporal evolution of the vertical cross-section at the University of Houston and La Porte in the Supplementary Materials (Fig. S5) and show the LES domain captures the peak low-level O_3 concentration (96 ppb) between 18:00 UTC (13:00 CDT) and 21:00 UTC (16:00 CDT) when compared to ground-based Lidar measurements from TRACER-AQ (90 - 125 ppb).

In addition, we compare the evolution of O_3 and NO_2 vertical profiles from the mesoscale domain D02 and LES domain D04

405 to show cross-domain differences in resolving variations of pollutants vertically (Fig. 7). As the day progresses, simulated O_3 mixing ratio near the surface increases, reaching up to 80 ppb in the LES domain in the late afternoon. In the early morning, O_3 increases while NO_2 decreases with height, indicating high O_3 accumulation aloft from the nocturnal stable layer and high NO_X emissions from surface anthropogenic activities during morning rush hours. A more well-mixed atmosphere during the daytime then reflects higher dispersion of pollutants from the surface to aloft. The inter-domain comparison shows contrasting

410 results in O_3 profile both below and above the PBL. O_3 in the LES domain D04 decreases with height within the PBL and gradually increases above 2 km, which is generally in line with lidar observations. More inter-domain comparison of diurnal evolution of vertical profiles of key meteorological and chemical factors are shown in Fig. S6. Following the comparative evaluation of the meteorology and chemistry across domains and between modeling and observations, the LES domain D04 provides a more realistic atmospheric condition.

415
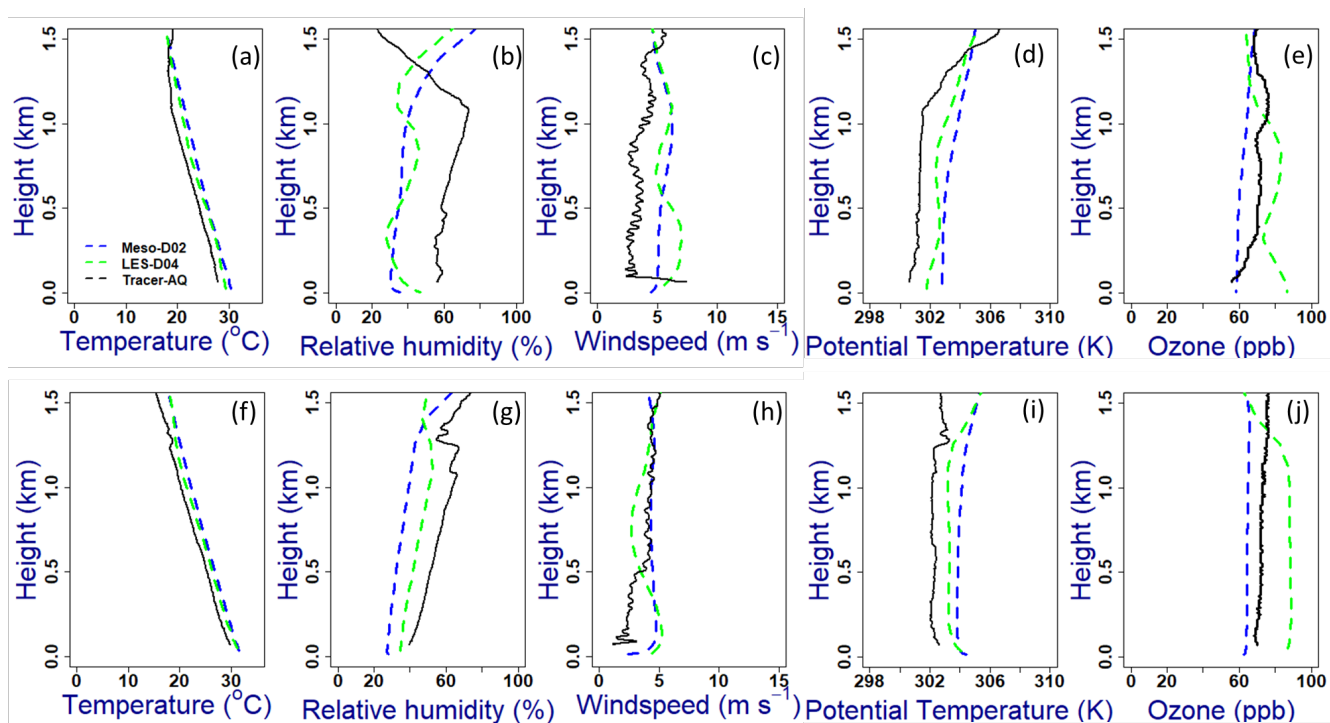
Figure 6: Comparison of vertical profiles of temperature, relative humidity, wind speed, potential temperature, and O₃ mixing ratio from the TRACER-AQ ozonesondes over Galveston Bay (12:47 CDT; a-e) and La Porte (13:07 CDT; f-j) with model results (13:00 CDT). The black lines represent observations; the blue dashed lines are for the D02 results with a resolution of 2700 m; the green dashed lines are for the LES D04 results with a resolution of 300 m.
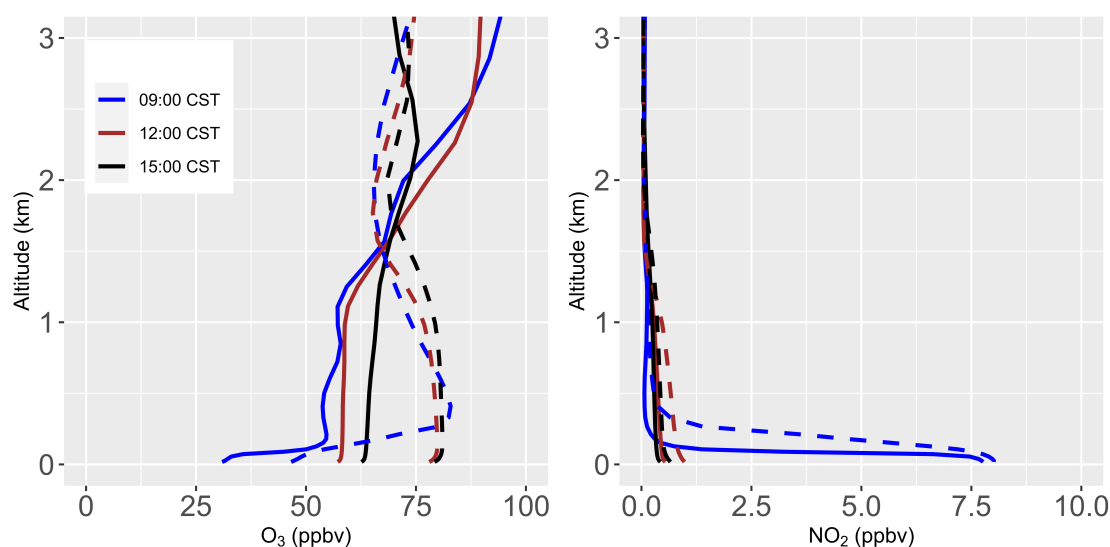
Figure 7: Domain-averaged vertical profiles of O₂ (left panel) and NO₂ (right panel) at 09:00 (blue), 12:00 (brown) and 15:00 CDT (black). Domain D02 results are shown as solid lines while the LES results over the D04 domain are represented as dashed lines.

3.3 O₃ formation regime

Next, we investigate the variability of O_3 production under different formation regimes. High O_3 production rate (PO₃) occurs in the Central Houston region and extends towards the Houston Ship Channel during the daytime (Fig S7). Previous studies have found that O_3 formation is driven by a non-linear photochemical reaction under NO$_X$-limited and VOC-limited regimes, and determined by different sensitivity indicators (Sillman et al., 2003; Ye et al., 2016). However, O_3 sensitivity indicators, including L_N/Q and FNR, may vary spatially and at different times due to the spatial and temporal heterogeneity of total radical loss via NO$_X$ and radical production as well as the mixing ratio of HCHO and NO_2 (Jin and Holloway, 2015). Figure 8 shows a spatial distribution of surface photochemical regimes associated with O_3 production from the simulated LES domain. Here, L_N/Q indicates O_3 production is mainly a VOC-limited regime ($L_N/Q > 0.5$) in the morning, and then transitions into a NO$_X$-limited regime ($L_N/Q < 0.5$) in the late afternoon. However, regions around Baytown, Texas City and Deer Park exhibit a VOC-limited or transitional regime also in the late afternoon. The FNR of the whole Houston area in the morning is less than 1.2, indicating that a VOC-limited regime is prevalent during this hour and a noontime transition into a NO$_X$-limited regime is also observed. It is worth noting that the transitional regime between a VOC-sensitive and NO$_X$-sensitive regime as defined by the FNR indicator varies with regions as described by Duncan et al. (2010). Previous findings by Schroeder et al. (2017) define the FNR transition regime over Houston between $0.7 < FNR < 2.0$, based on the relative rate of radical termination from radical-radical interactions to radical-NO$_X$ interactions. The ratio of FNR changes in response to the changes in VOCs and NO$_X$, and variations in NO_2 may have greater impacts on the ratio than variations in HCHO. Thus, it is difficult to define an explicit cut-off for the FNR transition regime based on fluctuations in NO_2. Ambient changes in HCHO and NO_2 respond immediately to changes in emissions sources and FNR will change in accordance, depending on which is predominant. Thus, using the ratio of radical production through HCHO and loss through NO$_X$ provides a more useful determinant for estimating FNR transition ratio of O_3 sensitivity. Hence, using model estimated values of the transition regime from the L_N/Q indicator, we calculated the threshold for FNR transition regime, and find a range of $0.6 < FNR < 1.8$ lies in the transition regime zone. Based on the similarities in the radical indicator approach to define the FNR transition regime, our associated range of FNR values is fairly consistent with the range described by Schroeder et al. (2017).

The discrepancy in our work compared to other studies relating to the modeled P(O_3) when using either L_N/Q or FNR may be attributed to differences in model chemistry and spatial resolution. Previous studies from Ren et al. (2013) and Mazzuca et al. (2016) used a simplified alkene chemistry in the Carbon Bond mechanism, version 5 (CB05) and overpredicted O_3 production in the morning in locations where alkenes dominate VOC reactivity. The alkene chemistry from the MOZART-T1 chemical mechanism used in our work considers relative alkene contributions from biogenic sources (Emmons et al., 2020), which is not often considered in other chemical mechanisms.

Figure 8: Spatial distributions of the O₃ formation regime determined by L_N/Q (upper panel) and FNR (lower panel) at 09:00 CDT, 12:00 CDT and 15:00 CDT. Calculated based on results from the LES domain over Houston.

The non-linear process of NO_2 and HCHO in relation to O_3 formation and sensitivity regimes is further discussed in Fig. 9 from the model simulations. In Fig. 9, PO_3 describes the rate of ozone production under different sensitivity regimes at specific diurnal hours while O_3 as a function of NO_2 and HCHO depicts the overall daytime concentration of O_3 under these regimes. In the morning, when NO_2 is high but HCHO is low, PO_3 is higher with increasing HCHO, indicating a VOC-limited regime. Though we note that the production rate of HO_X (OH + HO_2) radicals is lower than their loss rate during this period under high NO_2 concentrations, thus leading to a lower production of O_3 in the morning than in the afternoon. In the Supplementary Materials (Fig. S8), the maximum net PO_3 in the morning is estimated at 10 ppb h^{-1} over the whole of Houston. In contrast, during the afternoon when NO_2 is low but HCHO is high, PO_3 increases with increasing NO_2 levels and indicates a NO_X-limited regime. During this period, the rate of HO_X radical production is higher following the oxidation of VOCs by OH, thus

Figure 8: Spatial distributions of the O₃ formation regime determined by L_N/Q (upper panel) and FNR (lower panel) at 09:00 CDT, 12:00 CDT and 15:00 CDT. Calculated based on results from the LES domain over Houston.

The non-linear process of NO_2 and HCHO in relation to O_3 formation and sensitivity regimes is further discussed in Fig. 9 from the model simulations. In Fig. 9, PO_3 describes the rate of ozone production under different sensitivity regimes at specific diurnal hours while O_3 as a function of NO_2 and HCHO depicts the overall daytime concentration of O_3 under these regimes. In the morning, when NO_2 is high but HCHO is low, PO_3 is higher with increasing HCHO, indicating a VOC-limited regime. Though we note that the production rate of HO_X (OH + HO_2) radicals is lower than their loss rate during this period under high NO_2 concentrations, thus leading to a lower production of O_3 in the morning than in the afternoon. In the Supplementary Materials (Fig. S8), the maximum net PO_3 in the morning is estimated at 10 ppb h^{-1} over the whole of Houston. In contrast, during the afternoon when NO_2 is low but HCHO is high, PO_3 increases with increasing NO_2 levels and indicates a NO_X-limited regime. During this period, the rate of HO_X radical production is higher following the oxidation of VOCs by OH, thus

enhancing PO_3 in the afternoon. An increase in HO_2 reaction rate under a NO_X-limited regime leads to the enhancement of O_3 production (Li et al., 2023). The dependence of O_3 concentrations on NO_X levels during daytime chemistry shows that the O_3

470   mixing ratio is a maximum when NO_X levels are low (< 10 ppbv; Fig. S8). PO_3 reaches 50 ppb h^{-1} in the late afternoon, which is higher than the average afternoon O_3 production of 20 - 30 ppb h^{-1} observed during the DISCOVER-AQ campaign (Mazzuca et al., 2016). This further shows the high O_3 production during the TRACER-AQ campaign in 2021. The distinction, however, between these photochemical regimes is not simple and may be influenced by meteorology or unique environmental characteristics (De Foy et al., 2020; Li et al., 2023).

475
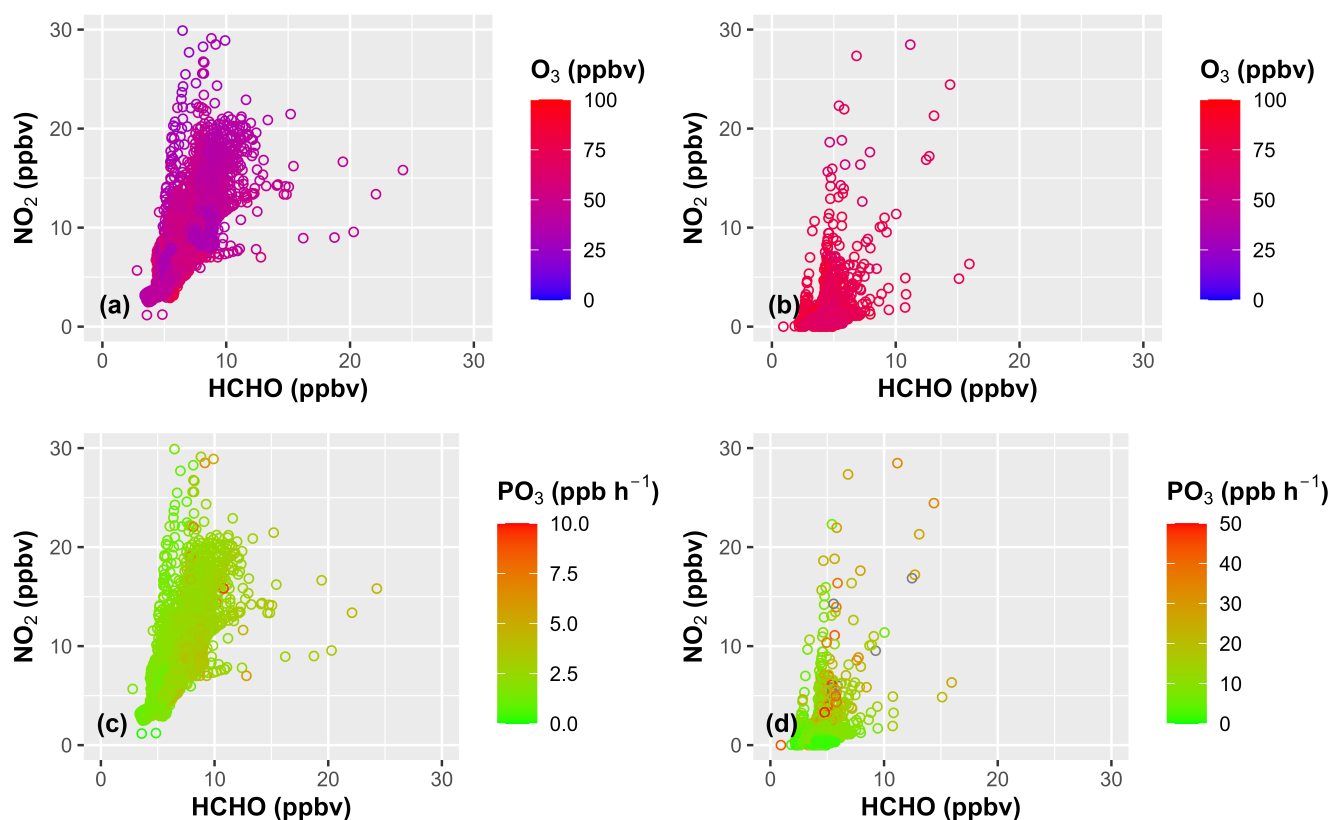
Figure 9: O_3 (upper panel) and PO_3 (lower panel) as a function of NO_2 and HCHO for 09:00 CDT (a and c) and 15:00 CDT (b and d) in Houston from the LES domain. NOTE: we use different color scales for morning and afternoon periods for distinct understanding of ozone formation at different times.

480

Since the observed NO_X-O_3-VOC chemistry in Fig. 8 shows some spatial heterogeneity of the O_3 sensitivity regimes, we further examine the photochemical production of O_3 in relation to different environments over Houston. Figure 10 shows the diurnal variability of O_3 and NO_X and the O_3 sensitivity regime indicators over four regions including Central Houston, La Porte, Brazoria-Galveston region (BGR) and the whole of Houston. According to Hossan et al. (2021), the contributions from

485   point sources in La Porte, Texas City near Galveston and downtown Houston contribute most to O_3 formation as point sources alongside other mobile sources. The stations also represent different pollution characteristics to understand how unique emission sources affect the overall photochemical sensitivity to PO_3. For example, heavy power plants contribute the most NO_X in a VOC-limited regime and transportation in a NO_X-limited regime (Jin and Holloway, 2015). According to Nowlan et al. (2018), the highest NO_X emissions in Houston are from the metropolitan area from mobile sources. Among other HRVOCs,

490   light olefins (including butene, ethane and propane) emissions dominate La Porte and Houston Ship Channel from petrochemical plants (Murphy and Allen, 2005). We show that NO_X levels are highest (NO_2 = 26 ppbv; NO = 6 ppbv) during the early morning over La Porte, followed by Central Houston (NO_2 = 22 ppbv; NO = 6 ppbv) and lowest at the Brazoria-Galveston region. The high level of NO_X over La Porte is mainly due to emissions from petrochemical plants and marine vessels at the HSC (Kim et al., 2011) and other mobile sources. On the other hand, NO_X emissions over Central Houston are

495   from mobile sources (Nowlan et al., 2018; Kim et al., 2011), while the NO_X levels from BGR can be attributed to petroleum refining sources around Texas City (Souri et al., 2018). Notably, NO_X levels are generally low from the late morning hours into the afternoon and underline the diurnal variability of NO_X emission sources as well as the fast photodissociation of NO_X. Although the NEI anthropogenic emissions inventory reasonably captures these diurnal patterns, improvements are further needed given its overestimation of NO_X in Houston.

500   The diurnal variation of L_N/Q and FNR indicates that O_3 formation is mainly a VOC-limited regime in the early morning over the Central Houston, La Porte and Whole Houston (domain average), and then transitions into a NO_X-limited regime later in the day (Fig. 10). During the morning hours, the lower O_3 mixing ratio in Central Houston and La Porte is mainly associated with a VOC-limited regime due to higher NO_X levels; however, they increase gradually towards noontime as NO_X decreases with increasing VOCs. This is consistent with previous studies that have shown that O_3 production is mainly suppressed by

505   high NO_X concentrations in a VOC-limited regime (Li et al., 2011). On average, O_3 formation is mainly NO_X-limited in the afternoon (between 11:30 and 16:00 CDT) across all the regions, and the high O_3 (Fig. 10) is dependent on the daytime abundance of RO_2 and HO_2 radicals through the photolysis of O_3, HCHO and other secondary VOCs (Ma et al., 2022). In the Brazoria-Galveston region, the high O_3 in the early morning hours is associated with O_3 production being mainly NO_X-limited between 6:30 and 7:30 CDT ($L_N/Q < 0.5$) before transitioning to a VOC-limited regime in the remaining hours of the morning

510   (8:00 and 11:30 CDT). During this NO_X-limited period, high sources of NO_2 rapidly increases O_3 formation (Duncan et al., 2010; Schroeder et al., 2017). In addition, we show how O_3 formation regime may vary spatially with height in the Supplementary Information (Fig. S9). We find that the production of O_3 is under a VOC-limited regime at the surface in the morning and transitions into a NO_X-limited regime in the upper atmosphere (> 200 m AGL) due to the rapid photochemical consumption nature of NO_X near the surface.

515
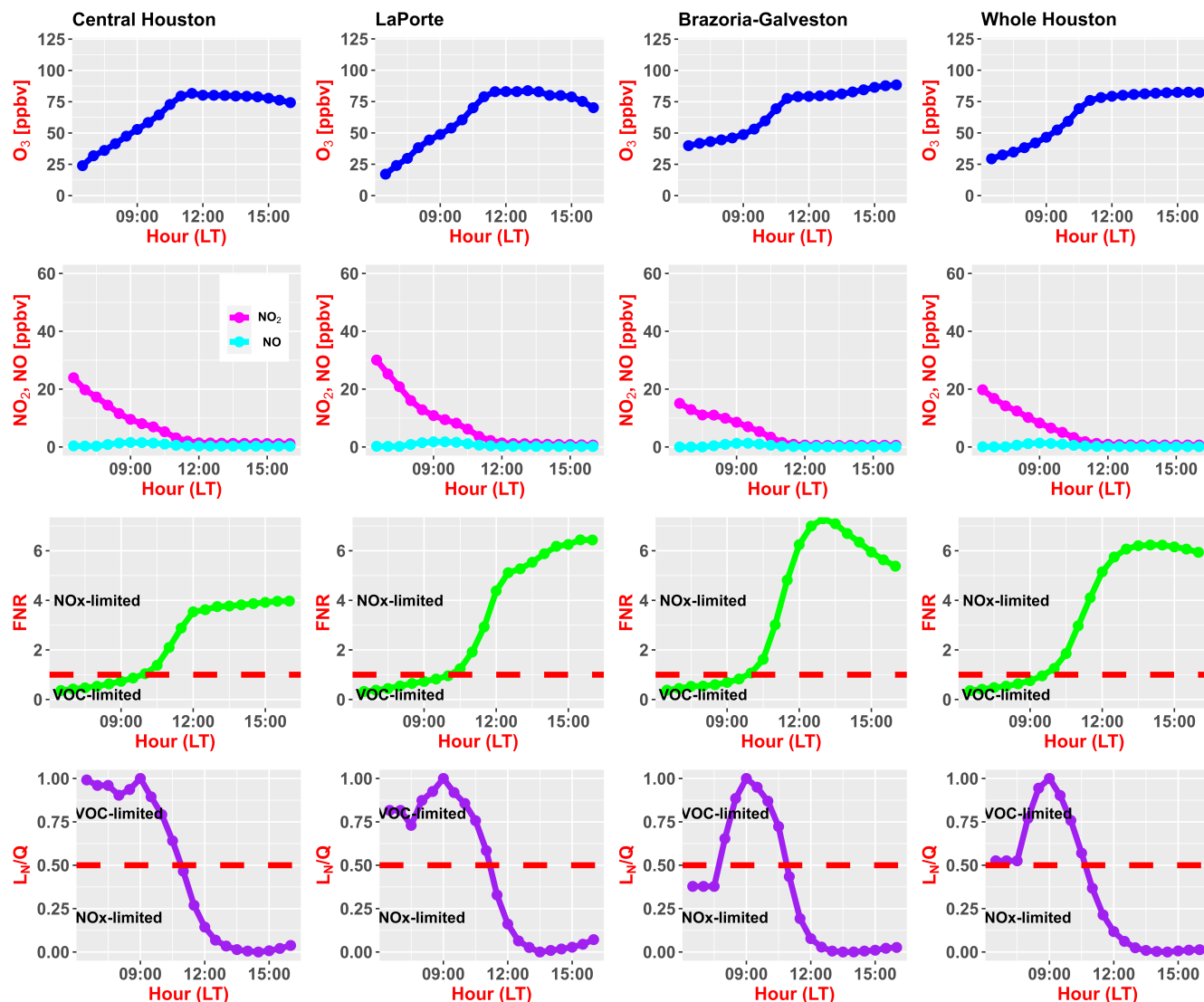
Figure 10: Diurnal variations of O₃ (first row), NO and NO₂ (second row), FNR (third row) and L_N/Q (fourth row) in the near-surface layer averaged over Central Houston (first column), La Porte (second column), Brazoria-Galveston (third column) and the whole LES domain (fourth column). Results are from the LES domain (D04).

3.4 OH reactivity

We further quantify the total OH reactivity (K_{OH}) to characterize the roles of VOCs in the formation of O₃. K_{OH} is defined as the sum of concentrations of OH reactants multiplied by their reaction rate coefficients (Yang et al., 2016; Fuchs et al., 2017; Ma et al., 2022), as shown in Eq. (4)

$$K_{OH} = \sum_i^n K_{VOC_i} \times [VOC_i] \qquad (4)$$

525   where [VOC$_i$] is the VOC concentrations and K$_{VOC_i}$ is the corresponding reaction rate coefficients. In this study, K$_{OH}$ is
        calculated from 29 major modeled VOC species which are grouped into three groups, including non-methane VOCs
        (NMVOCs), OVOCs and biogenic VOCs (BVOCs). The NMVOCs consist of alkanes (ethane, propane and lumped alkanes
        with C > 3), alkenes (ethene, propene/propylene, lumped alkenes with C > 3), alkynes (acetylene), aromatics (benzene, toluene,
        xylene) and glyoxal, while the BVOCs include isoprene and monoterpenes (limonene, α-pinene, β-pinene, β-caryophyllene

530   and other sesquiterpenes). The OVOCs species are mainly secondary VOC species and include ketones (methyl vinyl ketone,
        methyl ethyl ketone, acetone), aldehydes (formaldehyde, acetaldehyde, methacrolein, benzaldehyde, glycolaldehyde, lumped
        aldehyde), acids (formic acid, acetic acid), and alcohols (methanol, ethanol and phenol). Table 1 provides a summary of the
        total OH, O$_3$ and NO$_3$ reactivity with individual VOC species. The OH reactivity analysis shows isoprene is the highest
        contributor to total K$_{OH}$ at noon (12:00 CDT) at 9.86 s^{-1} (35.76 %), followed by CO (12.98 %), HCHO (12.21 %), Bigalk

535   (lumped alkanes; 6.29 %), and NO$_2$ (4.46 %). The contribution of the daytime reactivity of isoprene to the total K$_{OH}$ is
        substantial and very high when compared to other urban studies by Fuchs et al. (2017, 20 %) and Ma et al. (2022, 5 %). The
        contribution of HCHO (12.21 %) and acetaldehyde (4.88 %) as the most dominant OVOC species in reactivity with OH is
        consistent with the established literature from other locations (Whalley et al., 2016; Ma et al., 2022). Also, the high value of
        HCHO reactivity is related to the high values from the oxidation of isoprene, as HCHO in the Houston-Brazoria region is

540   predominantly from VOC oxidation (Parrish et al., 2012; Zhou et al., 2014). For most species, the modeled K$_{OH}$ reduces at
        15:00 CDT compared to the noontime, while isoprene was higher at 15:00 CDT (9.98 s^{-1}; 46.61 %). In addition, we consider
        the modeled reactivity of O$_3$ and NO$_3$ with VOCs and show that the total O$_3$ reactivity is dominated by the BVOCs. For
        example, the ozonolysis of β-caryophyllene increases from 0.39 s^{-1} at noon to 0.84 s^{-1} (27.07 %) in the late afternoon, due to
        the increased concentration of O$_3$ at 15:00 CDT.

545   The overall breakdown of the VOC groups and their OH reactivity over the focused regions averaged from 6:30 to 16:00 CDT
        is summarized in Fig. 11. The daytime total VOC concentration is dominated by OVOCs (73 %), while BVOCs contribute the
        least (~ 3 %). In comparison to other regions, the maximum VOC concentration is observed in La Porte. On the other hand,
        the total K$_{OH}$ is dominated by BVOCs (58 %) in the Central Houston region. From individual VOC species, NMVOCs species
        are mostly dominant with alkanes contributing to about 50–55 % of the total mixing ratio but are less reactive with OH radicals,

550   while alkenes are more reactive with OH radicals and contribute 60-65 % of the total K$_{OH}$ from NMVOCs across all zones.
        For BVOCs, isoprene is highly dominant with monoterpenes contributing less than 2 % in the total BVOC mixing ratio and
        reactivity with OH and mixing ratio. Aldehydes are the most reactive OVOCs (70-73 %), and alcohols dominate the total
        OVOC concentration (~50 %).

        Figure 12 shows the mixing ratio and OH reactivity of individually modeled compounds as a stacked area plot over the whole

555   Houston region. In the daytime, isoprene as the main biogenic species accounted for more than half of the total reactivity,
        while VOCs from anthropogenic activities and in oxygenated forms including alkanes, alkenes, aldehydes, alcohols and
        aromatics account for the other 50 % of the total OH reactivity. For NMVOCs and OVOCs, the total OH reactivity peaks at
        about 11:00 (CDT), while the OH reactivity of isoprene increases continuously during the day and peaks at 16:00 CDT. For

the mixing ratio, the NMVOCs peak in the early morning hours and gradually reduce towards late afternoon. Similar stacked
560   area plots for Central Houston, La Porte and the BGR are provided in the Supplementary Materials (Fig. S10-S12). The results
are consistent with the diurnal patterns observed over the whole Houston area, but a higher magnitude for total OH reactivity
of NMVOCs and OVOCs is observed in La Porte, while isoprene contributes the highest to the total K_{OH} in Central Houston.
The analysis of OH reactivity with VOC is important to estimate the potential of O_3 formation from VOC oxidation. The
oxidation of VOC by OH produces RO_2 and HO_2 radicals, which is identified as the major contributor to O_3 formation in
565   Houston (Zhou et al., 2014). While we show that isoprene contributes the highest to the total K_{OH} due to its high reactivity
with OH, it is unknown how much this affects O_3 formation. A recent study from Li et al. (2023) shows that isoprene reactivity
did not increase during high O_3 events during the NASA TRACER-AQ campaign, and shows similar OH reactivity on clean
O_3 days. OVOCs, similarly, show a high contribution to the total OH reactivity, particularly from HCHO and acetaldehyde,
however, they are considered the most important VOC species oxidized by OH that increases O_3 production (Zhou et al., 2014;
570   Li et al., 2023). According to previous studies in Houston, HCHO represents the highest contributor to HO_2 production (Parrish
et al., 2012; Ren et al., 2013; Wong et al., 2013). From the Supplementary Material (Table S2), we also show the photolysis
of HCHO, methyl glyoxal and glyoxal dominates the production of HO_X radicals over the whole Houston region. HCHO loss
rate through photolysis peaks (with a maximum of 0.14 pptv s^{-1}) at 12:00 CDT, similar to other loss rates across cities in
Europe at 0.28 pptv s^{-1} (Nussbaumer et al., 2021). Industrial emissions are identified as the main primary source of HCHO in
575   the Houston area (Johansson et al., 2014) with an average emission over the Houston region estimated at 8631.02 mol km^{-2} hr^{-1} over the simulation period based on the NEI inventory. In contrast, a comprehensive chemical analysis of airborne and ground
measurements of HCHO and emissions data concluded that HCHO is mainly from VOC oxidation in the Houston area (Parrish
et al., 2012). As HCHO is one of the major oxidation products of isoprene by OH (Sprengnether et al., 2002), we conclude
that high isoprene reactivity with OH enhances HCHO formation; the photolysis of HCHO forms HO_2 which then increases
580   the potential of O_3 formation.

Table 1: Reactivity of OH, O_3, and NO_3 with key chemical species (s^{-1}) averaged over the LES domain.

HRVOC Groups	Species	OH reactivity		O_3 reactivity		NO_3 reactivity	
		12:00 Noon	15:00 CDT	12:00 Noon	15:00 CDT	12:00 Noon	15:00 CDT
NMVOCs	Methane	0.29165	0.215078	-*	-	-	-
	Ethane	0.003451	0.002297	-	-	-	-
	Propane	0.008885	0.004246	-	-	-	-
	Bigalk (C_5H_{12})	0.481717	0.630683	-	-	-	-
	Ethene	0.202339	0.095153	0.016405	0.014473	-	-
	Propene	0.087006	0.047582	0.013262	0.015315	0.000033	0.000018
	Bigene (C_4H_8)	0.053194	0.042853	-	-	0.000394	0.000296
	Acetylene/Propylene	0.000193	0.000122	-	-	-	-
	Benzene	0.001054	0.000575	-	-	-	-
	Toluene	0.032341	0.011311	-	-	-	-
	Xylene	0.025272	0.009502	-	-	-	-
OVOCs	Formaldehyde	0.934925	0.486296	-	-	0.000076	0.000034

	Acetaldehyde	0.374008	0.165279	-	-	0.000066	0.000026
	Methacrolein	0.127278	0.098421	0.002455	0.003566	-	-
	Benzaldehyde	0.002014	0.000886	-	-	-	-
	Glycolaldehyde	0.086827	0.076907	-	-	-	-
	Methyl ethyl ketone	0.026124	0.012443	-	-	-	-
	Methyl vinyl ketone	0.058917	0.0486	0.006997	0.009998	-	-
	Acetone	0.020977	0.013498	-	-	-	-
	Acetic acid	0.011161	0.007475	-	-	-	-
	Formic acid	0.000758	0.000822	-	-	-	-
	Methanol	0.254674	0.166337	-	-	-	-
	Phenol	0.000364	0.000221	-	-	-	-
	Ethanol	0.154746	0.065338	-	-	-	-
	2-methyl-3-buten-2-ol (MBO)	-	-	0.000112	0.000197	-	-
	Glyoxal	0.036711	0.023485	-	-	-	-
	Methylglyoxal	0.079254	0.044156	-	-	0.000019	0.000009
BVOCs	Isoprene	2.738534	2.772071	0.271831	0.5330888	0.028773	0.02584423
	Limonene	0.014099	0.013134	0.011429	0.01969507	0.001292	0.00109182
	α-pinene	0.007128	0.00584	0.007377	0.01115669	0.001146	0.00082383
	β-pinene	0.006993	0.005868	0.001247	0.00197046	0.000317	0.00023717
	β-caryophyllene and other sesquiterpenes ($C_{15}H_{24}$)	0.003188	0.003879	0.109703	0.23419166	0.00041	0.00044159
Other trace species	CO	0.994169	0.644294	-	-	-	-
	SO_2	0.062321	0.026949	-	-	-	-
	O_3	0.124186	0.094638	-	-	-	-
	NO_2	0.341709	0.101966	-	-	0.044032	0.00924
	NO	-	-	-	-	0.152788	0.041117

Bigalk represents lumped alkanes with C > 3, and BIGENE for lumped alkenes with C > 3.

-* also represents chemical reactivity not included in the model chemical mechanism)
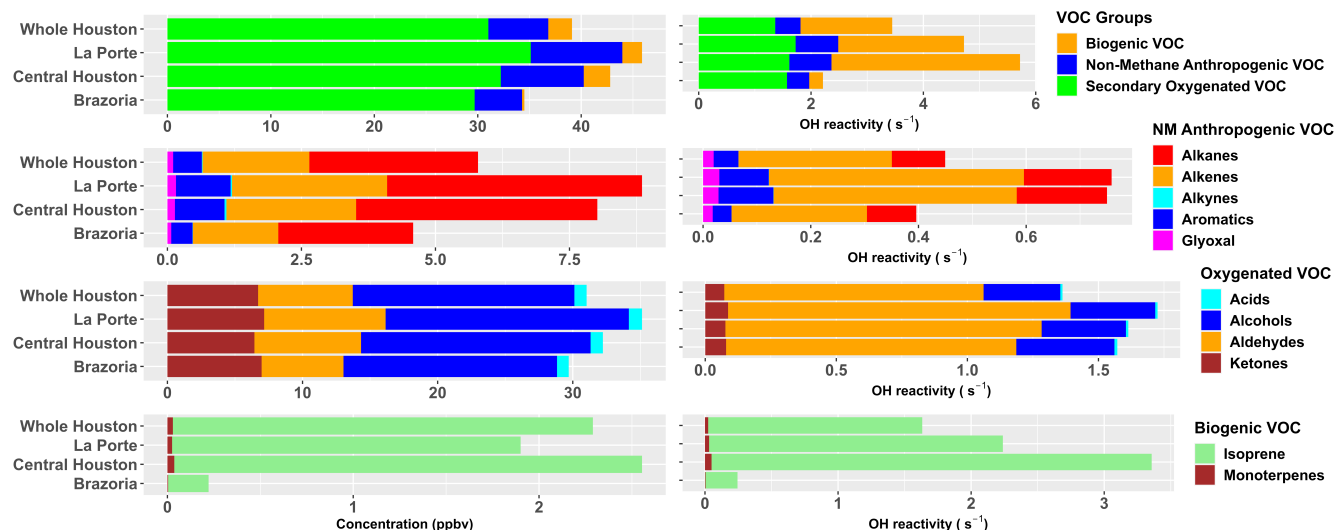
Figure 11: The breakdown of grouped VOC mixing ratio (left panel) and OH reactivity (right panel) averaged over Central Houston, La Porte, Brazoria-Galveston and the whole LES domain.
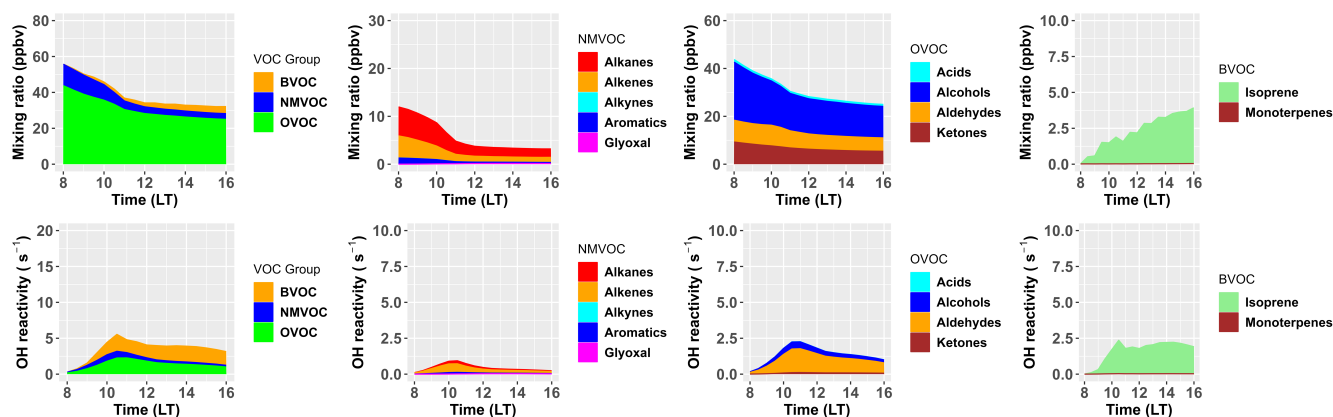
Figure 12: Diurnal variations of VOC mixing ratio (upper panel) and OH reactivity (lower panel) averaged over the LES domain for (a, e) the all-VOC group, (b, f) NMVOC, (c, g) OVOC and (d, h) BVOC.

3.5 AOC analysis

The oxidative capacity of the atmosphere is important to understand the abundance of RO_X radicals including HO_2, OH and RO_2 radicals, which drive the production, transformation and recycling of O_3 (Liu et al., 2022). AOC is calculated as the sum of oxidation rates of various pollutants by the major oxidants (OH, NO_3 and O_3) (Xue et al., 2016; Chen et al., 2020; Liu et al., 2022). In this study, AOC is calculated based on the modeled VOCs and their rate coefficients, as shown in Eq. (5-7), and does not account for the reactivity of OH, NO_3 and O_3 with other VOC oxidation products that are not included in the gas phase mechanism used within our WRF-LES-Chem modeling. Thus, we acknowledge that possible discrepancies may exist between

the calculated values of these reactivities and their actual measurements, as shown in previous studies (Mao et al., 2010; Ren et al., 2013).

$$Total\ OH\ reactivity = \begin{matrix} \sum k_{OH+NMVOC_i}[NMVOC_i] + \\ k_{OH+CH_4}[CH_4] + k_{OH+CO}[CO] + \\ k_{OH+NO}[NO] + k_{OH+NO_2}[NO_2] + \\ k_{OH+SO_2}[SO_2] + k_{OH+O_3}[O_3] + \cdots \end{matrix} \tag{5}$$

$$Total\ O_3\ reactivity = \begin{matrix} \sum k_{O_3+NMVOC_i}[NMVOC_i] + \\ k_{O_3+CH_4}[CH_4] + k_{O_3+NO}[NO] + \\ k_{O_3+NO_2}[NO_2] + \cdots \end{matrix} \tag{6}$$

$$Total\ NO_3\ reactivity = \begin{matrix} \sum k_{NO_3+NMVOC_i}[NMVOC_i] + \\ k_{NO_3+CH_4}[CH_4] + k_{NO_3+NO}[NO] + \\ k_{NO_3+NO_2}[NO_2] + k_{NO_3+SO_2}[SO_2] + \cdots \end{matrix} \tag{7}$$

Figure 13 shows the time series of the model-calculated AOC over Houston. The estimated AOC daytime averages (08:00 – 16:00 CDT) is 1.11 x 10^8 molecules cm^{-3} s^{-1}, 0.88 x 10^8 molecules cm^{-3} s^{-1}, 0.52 x 10^8 molecules cm^{-3} s^{-1} and 0.69 x 10^8
605 molecules cm^{-3} s^{-1} respectively for Central Houston, La Porte, Brazoria-Galveston and Whole Houston. As shown in Fig. 13, the daily maximum AOC is observed in Central Houston and La Porte at 1.5 x 10^8 molecules cm^{-3} s^{-1}, and much higher than those in the less polluted region in Brazoria-Galveston at 0.8 x 10^8 molecules cm^{-3} s^{-1}. The daily maximum AOC is similar to other areas with high pollution from oil and gas in China (1.8 x 10^8 molecules cm^{-3} s^{-1}; Chen et al., 2020) or other urban areas in Hong Kong (1.3 x 10^8 molecules cm^{-3} s^{-1}; Xue et al., 2016) or Xiamen (1.3 x 10^8 molecules cm^{-3} s^{-1}; Liu et al., 2022).
610 The differences in AOC across these regions may be attributed to relatively higher solar radiation or pollutant concentrations among different sites (Zhu et al., 2020; Liu et al., 2022). As expected, OH is the major daytime oxidant, accounting for more than 90 % of the total AOC. In the late afternoon, the contribution of O_3 to AOC increases up to 8-10 % in Central Houston and La Porte compared to the morning hours when they contribute less than 5 %. In addition, the higher contribution of O_3 to AOC is attributed to the high concentration of alkenes in the region (Xue et al., 2016), and alkene ozonolysis increases as the
615 day progresses with the abundance of O_3. AOC contributed by NO_3 is negligible as NO_3 can be quickly photodissociated during daytime thus having a low daytime concentration. Figure 14 elucidates the daytime variability of primary anthropogenic VOCs, OVOCs and trace species and their reactivity with OH, O_3 and NO_3. In Brazoria-Galveston, the oxidation of alkanes, CO and methane (CH_4) by OH increases slightly as the day progresses into late afternoon. The simulated OVOCs are the dominant contributor to OH reactivity and contribute 30-40 % of the total AOC across all regions. This is similarly evident
620 over the whole of Houston. Further information from the Supplementary material shows that the total OH reactivity for OVOCs is much higher (1.36 ± 0.59 s^{-1}) (mean ± standard deviation) on average over the whole domain compared to other groups (see Table S3), while CO (0.72 ± 0.29 s^{-1}), CH_4 (0.2 ± 0.09 s^{-1}), alkanes (0.3 ± 0.12 s^{-1}), alkenes (0.28 ± 0.16 s^{-1}), aromatics (0.05 ± 0.03 s^{-1}), and SO_2 (0.04 ± 0.02 s^{-1}) also make up the averaged total OH reactivity, thus indicating the strong influence of anthropogenic emissions in Houston. The comparison across different zones shows that the oxidation of alkanes (0.39 ± 0.19

625   s^{-1}), aromatics (0.1 ± 0.07 s^{-1}), and CO (0.93 ± 0.47 s^{-1}) is highest over Central Houston, while the oxidation of alkenes (0.47 ± 0.30 s^{-1}) and SO$_2$ (0.06 ± 0.04 s^{-1}) is mostly dominant over La Porte. In contrast, the OH reactivity via CH$_4$ oxidation (0.27 ± 0.13 s^{-1}) is the highest over the BGR region. CH$_4$ represents an important factor that affects AOC, with OH + CH$_4$ being an important sink for OH in the atmosphere (Morgenstern et al., 2013). Overall, this underlines the role of spatial characteristics and unique local anthropogenic emission sources, which may contribute to the overall photochemical processes.

630
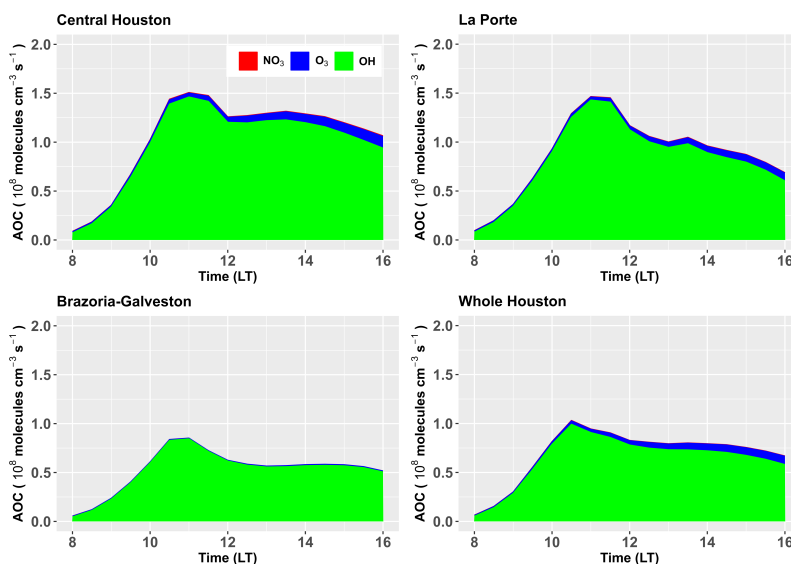
Figure 13: Diurnal variations of AOC averaged over the Central Houston, La Porte, Brazoria-Galveston and the whole LES domain. Results are from the LES -domain.
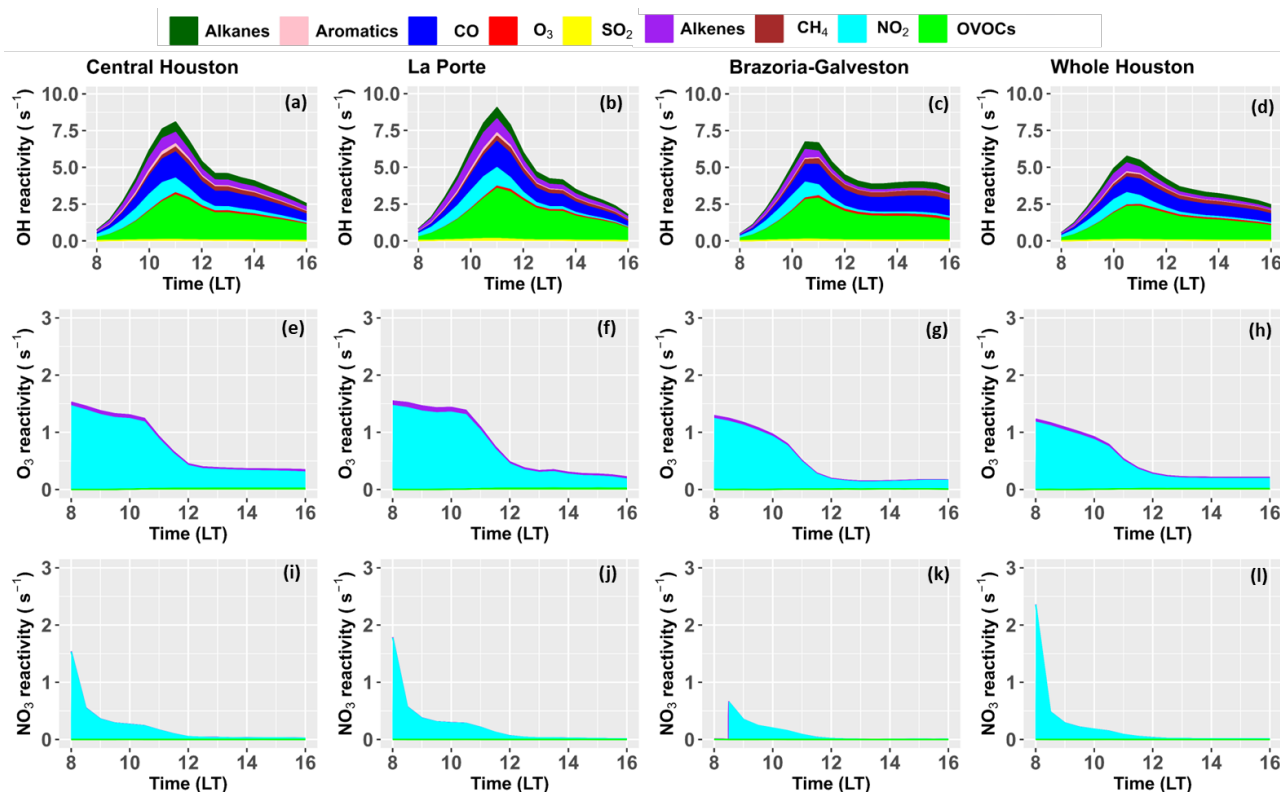
Figure 14: Diurnal variations of OH reactivity (a-d), O₃ reactivity (e-h), and NO₃ reactivity (i-l) of selected major anthropogenic chemicals averaged over the Central Houston (first panel), La Porte (second panel), Brazoria-Galveston (third panel) and the whole LES domain (fourth panel). Results are from the LES domain.

4. Conclusion

In this study, we investigate the detailed atmospheric photochemistry during a high O_3 episode during TRACER-AQ 2021 in Houston. During this episode, observed surface O_3 significantly exceeded national standards by 20-50 ppb, particularly in the Central areas of Houston. We use a high-resolution WRF-LES-Chem model to simulate atmospheric O_3 as well as the detailed atmospheric photochemistry associated with these O_3 exceedances. By resolving turbulence and eddies at a scale relevant for pollutant chemistry, the LES simulation 300 m spatial resolution adequately captures the surface concentration of O_3, NO_X, and HCHO, and provides an improved representation of temperature, wind speed and water vapor compared to the mesoscale WRF-Chem simulations.

Two indicators for the O_3 sensitivity regime (L_N/Q and FNR) are compared and show that the photochemical properties of O_3 formation in Houston is largely a VOC-limited regime in the morning hours and transitions into a NO_X-limited regime in the afternoon. Additionally, the transition threshold for radical loss-initiation ratio, L_N/Q, is used to define the FNR transition regime, which is observed at $0.6 < FNR < 1.8$. Some local regions, including Baytown, Texas City and Deer Park show no diurnal variability in O_3 formation sensitivity regimes, due to unique environmental and emission sources. On September 8,

2021, the rapid radical production and recycling of HO_X radicals and their reactivity with increased VOC emissions and reduced NO_2 emissions under a NO_X-limited regime accelerated fast and high O_3 production. The total radical production rate of HO_X radicals increased PO_3 in the afternoon hours, reaching 50 ppb h^{-1}, and higher than the previously recorded average in the DISCOVER-AQ campaign.

655 Increased HRVOC emission is the main cause of radical production. The HO_2 radical is mainly formed from the oxidation of HCHO and represents the highest source of HO_2 in Houston. The oxidation of other OVOCs including acetaldehyde also enhances the production of HO_2 radicals, which contributes to increased O_3 production. Our analysis linked the high oxidation of isoprene to enhance the production of HCHO, thus increasing the potential of O_3 formation when oxidized by OH. Our results further underline the role of BVOCs and how they may account for enhanced O_3 production, which is consistent with

660 some recent studies (Leong et al., 2017; Ma et al., 2022). Similarly, RO_2 sources are alkenes oxidation, as compared to the oxidation of alkanes and aromatics.

Overall, the role of anthropogenic emissions cannot be underestimated. Primary emissions of CO and non-methane hydrocarbons (alkenes and other alkanes) affect the overall AOC levels, though the contribution of each compound to AOC varies with location and time. OVOCs also contribute about 30-40 % to the total AOC. Our study thus concludes the important

665 role of anthropogenic emissions in the production of RO_2 and HO_2 radicals, and how they may influence the enhancement or inhibition of O_3 formation, depending on the NOx-O_3-VOC sensitivity regimes. This suggests the importance of further reductions in highly reactive anthropogenic VOCs to achieve further reductions in O_3 levels.

Code and data availability

670 The source code of WRF-Chem is publicly available on GitHub at https://github.com/wrf-model/WRF. Observational data from TCEQ and Pandora can be downloaded from the TAMIS web interface (https://www17.tceq.texas.gov/tamis/index.cfm; last access: 30 June 2023) and the Pandonia Global Network (https://www.pandonia-global-network.org/; last access: 3 July 2023) respectively. The TRACER-AQ data is archived on the NASA webpage (https://www-air.larc.nasa.gov/cgi-bin/ArcView/traceraq.2021). The Lidar data from the TRACER-AQ campaign is also available on the NASA Tropospheric

675 Ozone Lidar Network (https://tolnet.larc.nasa.gov).

Authors contributions

AF performed the simulations, carried out the analyses and wrote the manuscript. YL conceived and supervised the study and revised the paper. JD provided guidance in modeling setup and contributed to the editing of the paper. RS, SU, PW, JS, GG, JF, ME and TG provided measurement datasets and contributed to the editing of the paper.

Competing interests

The authors have declared no competing interests.

Disclaimer

No Disclaimer.

Acknowledgements

This research is funded by Baylor Universtiy. We acknowledge the contributions of the individuals and research groups who have collected and publicly shared their data from the TRACER-AQ 2021 campaign. We also acknowledge all the valuable suggestions from the scientists at NCAR and NOAA, including Dr. Mary Barth, Dr. Ned Patton, and Dr. Siyuan Wang. The San Jacinto field measurements and data analysis were funded by the Texas Commission on Environmental Quality (TCEQ, 582-21-22179-015 and 582-22-31913-020). The content, findings, opinions, and conclusions are the work of the authors and do not necessarily represent the findings, opinions, or conclusions of the TCEQ.

References

Baek, K., Kim, J. H., Herman, J. R., Haffner, D. P., and Kim, J.: Validation of Brewer and Pandora measurements using OMI total ozone, Atmos. Environ., 160, 165–175, https://doi.org/10.1016/j.atmosenv.2017.03.034, 2017.

Banta, R. M., Senff, C. J., Alvarez, R. J., Langford, A. O., Parrish, D. D., Trainer, M. K., Darby, L. S., Michael Hardesty, R., Lambeth, B., Andrew Neuman, J., Angevine, W. M., Nielsen-Gammon, J., Sandberg, S. P., and White, A. B.: Dependence of daily peak O3 concentrations near Houston, Texas on environmental factors: Wind speed, temperature, and boundary-layer depth, Atmos. Environ., 45, 162–173, https://doi.org/10.1016/j.atmosenv.2010.09.030, 2011.

Berlin, S. R., Langford, A. O., Estes, M., Dong, M., and Parrish, D. D.: Magnitude, Decadal Changes, and Impact of Regional Background Ozone Transported into the Greater Houston, Texas, Area, Environ. Sci. Technol., 47, 13985–13992, https://doi.org/10.1021/es4037644, 2013.

Blanchard, C. L., Tanenbaum, S., and Lawson, D. R.: Differences between Weekday and Weekend Air Pollutant Levels in Atlanta; Baltimore; Chicago; Dallas–Fort Worth; Denver; Houston; New York; Phoenix; Washington, DC; and Surrounding Areas, J. Air Waste Manag. Assoc., 58, 1598–1615, https://doi.org/10.3155/1047-3289.58.12.1598, 2008.

Botlaguduru, V. S. V. and Kommalapati, R. R.: Meteorological detrending of long-term (2003-2017) ozone and precursor concentrations at three sites in the Houston Ship Channel Region, J. Air Waste Manag. Assoc., 70, 93–107, https://doi.org/10.1080/10962247.2019.1694088, 2020.

Botlaguduru, V. S. V., Kommalapati, R. R., and Huque, Z.: Long-term meteorologically independent trend analysis of ozone air quality at an urban site in the greater Houston area, J. Air Waste Manag. Assoc., 68, 1051–1064, https://doi.org/10.1080/10962247.2018.1466740, 2018.

710 Brown, S. S., Dubé, W. P., Peischl, J., Ryerson, T. B., Atlas, E., Warneke, C., de Gouw, J. A., te Lintel Hekkert, S., Brock, C. A., Flocke, F., Trainer, M., Parrish, D. D., Feshenfeld, F. C., and Ravishankara, A. R.: Budgets for nocturnal VOC oxidation by nitrate radicals aloft during the 2006 Texas Air Quality Study, J. Geophys. Res. Atmospheres, 116, https://doi.org/10.1029/2011JD016544, 2011.

Chen, D., Wang, Y., McElroy, M. B., He, K., Yantosca, R. M., and Le Sager, P.: Regional CO pollution and export in China

715 simulated by the high-resolution nested-grid GEOS-Chem model, Atmospheric Chem. Phys., 9, 3825–3839, https://doi.org/10.5194/acp-9-3825-2009, 2009.

Chen, F. and Dudhia, J.: Coupling an Advanced Land Surface–Hydrology Model with the Penn State–NCAR MM5 Modeling System. Part I: Model Implementation and Sensitivity, Mon. Weather Rev., 129, 569–585, https://doi.org/10.1175/1520-0493(2001)129<0569:CAALSH>2.0.CO;2, 2001.

720 Chen, T., Xue, L., Zheng, P., Zhang, Y., Liu, Y., Sun, J., Han, G., Li, H., Zhang, X., Li, Y., Li, H., Dong, C., Xu, F., Zhang, Q., and Wang, W.: Volatile organic compounds and ozone air pollution in an oil production region in northern China, Atmospheric Chem. Phys., 20, 7069–7086, https://doi.org/10.5194/acp-20-7069-2020, 2020.

Chen, X., Wang, H., Liu, Y., Su, R., Wang, H., Lou, S., and Lu, K.: Spatial characteristics of the nighttime oxidation capacity in the Yangtze River Delta, China, Atmos. Environ., 208, 150–157, https://doi.org/10.1016/j.atmosenv.2019.04.012, 2019.

725 Chen, Y., Wang, M., Yao, Y., Zeng, C., Zhang, W., Yan, H., Gao, P., Fan, L., and Ye, D.: Research on the ozone formation sensitivity indicator of four urban agglomerations of China using Ozone Monitoring Instrument (OMI) satellite data and ground-based measurements, Sci. Total Environ., 869, 161679, https://doi.org/10.1016/j.scitotenv.2023.161679, 2023.

Choi, Y. and Souri, A. H.: Chemical condition and surface ozone in large cities of Texas during the last decade: Observational evidence from OMI, CAMS, and model analysis, Remote Sens. Environ., 168, 90–101,

730 https://doi.org/10.1016/j.rse.2015.06.026, 2015.

Cuchiara, G. C., Li, X., Carvalho, J., and Rappenglück, B.: Intercomparison of planetary boundary layer parameterization and its impacts on surface ozone concentration in the WRF/Chem model for a case study in Houston/Texas, Atmos. Environ., 96, 175–185, https://doi.org/10.1016/j.atmosenv.2014.07.013, 2014.

Czader, B. H. and Rappenglück, B.: Modeling of 1,3-butadiene in urban and industrial areas, Atmos. Environ., 102, 30–42,

735 https://doi.org/10.1016/j.atmosenv.2014.11.039, 2015.

Darby, L. S.: Cluster analysis of surface winds in Houston, Texas, and the impact of wind patterns on ozone, J. Appl. Meteorol., 44, 1788–1806, https://doi.org/10.1175/JAM2320.1, 2005.

Deardorff, J. W.: A numerical study of three-dimensional turbulent channel flow at large Reynolds numbers, J. Fluid Mech., 41, 453–480, https://doi.org/10.1017/S0022112070000691, 1970.

740 De Foy, B., Brune, W. H., and Schauer, J. J.: Changes in ozone photochemical regime in Fresno, California from 1994 to 2018 deduced from changes in the weekend effect, Environ. Pollut., 263, 114380, https://doi.org/10.1016/j.envpol.2020.114380, 2020.

Dowell, D. C., Alexander, C. R., James, E. P., Weygandt, S. S., Benjamin, S. G., Manikin, G. S., Blake, B. T., Brown, J. M., Olson, J. B., Hu, M., Smirnova, T. G., Ladwig, T., Kenyon, J. S., Ahmadov, R., Turner, D. D., Duda, J. D., and Alcott, T. I.:

745 The High-Resolution Rapid Refresh (HRRR): An Hourly Updating Convection-Allowing Forecast Model. Part I: Motivation and System Description, Weather Forecast., 37, 1371–1395, https://doi.org/10.1175/WAF-D-21-0151.1, 2022.

Du, X., Tang, W., Zhang, Z., Li, Y., Yu, Y., Xiao, Z., and Meng, F.: Sensitivity modeling of ozone and its precursors over the Chengdu metropolitan area, Atmos. Environ., 277, 119071, https://doi.org/10.1016/j.atmosenv.2022.119071, 2022.

Duncan, B. N., Yoshida, Y., Olson, J. R., Sillman, S., Martin, R. V., Lamsal, L., Hu, Y., Pickering, K. E., Retscher, C., Allen,

750 D. J., and Crawford, J. H.: Application of OMI observations to a space-based indicator of NOx and VOC controls on surface ozone formation, Atmos. Environ., 44, 2213–2223, https://doi.org/10.1016/j.atmosenv.2010.03.010, 2010.

Emmons, L. K., Schwantes, R. H., Orlando, J. J., Tyndall, G., Kinnison, D., Lamarque, J.-F., Marsh, D., Mills, M. J., Tilmes, S., Bardeen, C., Buchholz, R. R., Conley, A., Gettelman, A., Garcia, R., Simpson, I., Blake, D. R., Meinardi, S., and Pétron, G.: The Chemistry Mechanism in the Community Earth System Model Version 2 (CESM2), J. Adv. Model. Earth Syst., 12,

755 e2019MS001882, https://doi.org/10.1029/2019MS001882, 2020.

Fast, J. D., Gustafson Jr., W. I., Easter, R. C., Zaveri, R. A., Barnard, J. C., Chapman, E. G., Grell, G. A., and Peckham, S. E.: Evolution of ozone, particulates, and aerosol direct radiative forcing in the vicinity of Houston using a fully coupled meteorology-chemistry-aerosol model, J. Geophys. Res. Atmospheres, 111, https://doi.org/10.1029/2005JD006721, 2006.

Faulstich, S. D., Schissler, A. G., Strickland, M. J., and Holmes, H. A.: Statistical Comparison and Assessment of Four Fire

760 Emissions Inventories for 2013 and a Large Wildfire in the Western United States, Fire, 5, 27, https://doi.org/10.3390/fire5010027, 2022.

Fuchs, H., Tan, Z., Lu, K., Bohn, B., Broch, S., Brown, S. S., Dong, H., Gomm, S., Häseler, R., He, L., Hofzumahaus, A., Holland, F., Li, X., Liu, Y., Lu, S., Min, K.-E., Rohrer, F., Shao, M., Wang, B., Wang, M., Wu, Y., Zeng, L., Zhang, Y., Wahner, A., and Zhang, Y.: OH reactivity at a rural site (Wangdu) in the North China Plain: contributions from OH reactants

765 and experimental OH budget, Atmospheric Chem. Phys., 17, 645–661, https://doi.org/10.5194/acp-17-645-2017, 2017.

Gettelman, A., Hannay, C., Bacmeister, J. T., Neale, R. B., Pendergrass, A. G., Danabasoglu, G., Lamarque, J.-F., Fasullo, J. T., Bailey, D. A., Lawrence, D. M., and Mills, M. J.: High Climate Sensitivity in the Community Earth System Model Version 2 (CESM2), Geophys. Res. Lett., 46, 8329–8337, https://doi.org/10.1029/2019GL083978, 2019.

Geyer, A., Alicke, B., Ackermann, R., Martinez, M., Harder, H., Brune, W., di Carlo, P., Williams, E., Jobson, T., Hall, S.,

770 Shetter, R., and Stutz, J.: Direct observations of daytime NO3: Implications for urban boundary layer chemistry, J. Geophys. Res. Atmospheres, 108, https://doi.org/10.1029/2002JD002967, 2003.

Gholami, S., Ghader, S., Khaleghi-Zavareh, H., and Ghafarian, P.: Sensitivity of WRF-simulated 10 m wind over the Persian Gulf to different boundary conditions and PBL parameterization schemes, Atmospheric Res., 247, 105147, https://doi.org/10.1016/j.atmosres.2020.105147, 2021.

775 Goldberg, D. L., Vinciguerra, T. P., Anderson, D. C., Hembeck, L., Canty, T. P., Ehrman, S. H., Martins, D. K., Stauffer, R. M., Thompson, A. M., Salawitch, R. J., and Dickerson, R. R.: CAMx ozone source attribution in the eastern United States using guidance from observations during DISCOVER-AQ Maryland, Geophys. Res. Lett., 43, 2249–2258, https://doi.org/10.1002/2015GL067332, 2016.

Goldberg, D. L., Harkey, M., de Foy, B., Judd, L., Johnson, J., Yarwood, G., and Holloway, T.: Evaluating NO_x emissions and
780 their effect on O_3 production in Texas using TROPOMI NO_2 and HCHO, Atmospheric Chem. Phys., 22, 10875–10900, https://doi.org/10.5194/acp-22-10875-2022, 2022.

Grant, L. D., Heever, S. C. van den, Haddad, Z. S., Bukowski, J., Marinescu, P. J., Storer, R. L., Posselt, D. J., and Stephens, G. L.: A Linear Relationship between Vertical Velocity and Condensation Processes in Deep Convection, J. Atmospheric Sci., 79, 449–466, https://doi.org/10.1175/JAS-D-21-0035.1, 2022.

785 Grell, G. A. and Dévényi, D.: A generalized approach to parameterizing convection combining ensemble and data assimilation techniques, Geophys. Res. Lett., 29, 38-1-38–4, https://doi.org/10.1029/2002GL015311, 2002.

Grell, G. A., Peckham, S. E., Schmitz, R., McKeen, S. A., Frost, G., Skamarock, W. C., and Eder, B.: Fully coupled "online" chemistry within the WRF model, Atmos. Environ., 39, 6957–6975, https://doi.org/10.1016/j.atmosenv.2005.04.027, 2005.

Gronoff, G., Robinson, J., Berkoff, T., Swap, R., Farris, B., Schroeder, J., Halliday, H. S., Knepp, T., Spinei, E., Carrion, W.,
790 Adcock, E. E., Johns, Z., Allen, D., and Pippin, M.: A method for quantifying near range point source induced O3 titration events using Co-located Lidar and Pandora measurements, Atmos. Environ., 204, 43–52, https://doi.org/10.1016/j.atmosenv.2019.01.052, 2019.

Guenther, A., Karl, T., Harley, P., Wiedinmyer, C., Palmer, P. I., and Geron, C.: Estimates of global terrestrial isoprene emissions using MEGAN (Model of Emissions of Gases and Aerosols from Nature), Atmospheric Chem. Phys., 6, 3181–3210,
795 https://doi.org/10.5194/acp-6-3181-2006, 2006.

Herman, J., Cede, A., Spinei, E., Mount, G., Tzortziou, M., and Abuhassan, N.: NO2 column amounts from ground-based Pandora and MFDOAS spectrometers using the direct-sun DOAS technique: Intercomparisons and application to OMI validation, J. Geophys. Res. Atmospheres, 114, https://doi.org/10.1029/2009JD011848, 2009.

Herman, J., Spinei, E., Fried, A., Kim, J., Kim, J., Kim, W., Cede, A., Abuhassan, N., and Segal-Rozenhaimer, M.: NO_2 and
800 HCHO measurements in Korea from 2012 to 2016 from Pandora spectrometer instruments compared with OMI retrievals and with aircraft measurements during the KORUS-AQ campaign, Atmospheric Meas. Tech., 11, 4583–4603, https://doi.org/10.5194/amt-11-4583-2018, 2018.

Herrmann, M. and Gutheil, E.: Simulation of the Air Quality in Southern California, USA in July and October of the Year 2018, Atmosphere, 13, 548, https://doi.org/10.3390/atmos13040548, 2022.

805   Hong, S.-Y., Noh, Y., and Dudhia, J.: A New Vertical Diffusion Package with an Explicit Treatment of Entrainment Processes, Mon. Weather Rev., 134, 2318–2341, https://doi.org/10.1175/MWR3199.1, 2006.

Hossan, I., Du, H., and Kommalapati, R. R.: Anthropogenic Source Contributions to Ozone Formation in the Greater Houston Area, J. Environ. Prot., 12, 249–264, https://doi.org/10.4236/jep.2021.124016, 2021.

Iacono, M. J., Delamere, J. S., Mlawer, E. J., Shephard, M. W., Clough, S. A., and Collins, W. D.: Radiative forcing by long-
810   lived greenhouse gases: Calculations with the AER radiative transfer models, J. Geophys. Res. Atmospheres, 113, https://doi.org/10.1029/2008JD009944, 2008.

Jiménez, P. A., Dudhia, J., González-Rouco, J. F., Navarro, J., Montávez, J. P., and García-Bustamante, E.: A Revised Scheme for the WRF Surface Layer Formulation, Mon. Weather Rev., 140, 898–918, https://doi.org/10.1175/MWR-D-11-00056.1, 2012.

815   Jiménez, P. A., Dudhia, J., Thompson, G., Lee, J. A., and Brummet, T.: Improving the cloud initialization in WRF-Solar with enhanced short-range forecasting functionality: The MAD-WRF model, Sol. Energy, 239, 221–233, https://doi.org/10.1016/j.solener.2022.04.055, 2022.

Jin, X. and Holloway, T.: Spatial and temporal variability of ozone sensitivity over China observed from the Ozone Monitoring Instrument, J. Geophys. Res. Atmospheres, 120, 7229–7246, https://doi.org/10.1002/2015JD023250, 2015.

820   Johansson, J. K. E., Mellqvist, J., Samuelsson, J., Offerle, B., Moldanova, J., Rappenglück, B., Lefer, B., and Flynn, J.: Quantitative measurements and modeling of industrial formaldehyde emissions in the Greater Houston area during campaigns in 2009 and 2011, J. Geophys. Res. Atmospheres, 119, 4303–4322, https://doi.org/10.1002/2013JD020159, 2014.

Kantha Rao, B. and Rakesh, V.: Evaluation of WRF-simulated multilevel soil moisture, 2-m air temperature, and 2-m relative humidity against in situ observations in India, Pure Appl. Geophys., 176, 1807–1826, https://doi.org/10.1007/s00024-018-
825   2022-7, 2019.

Kim, S.-W., McKeen, S. A., Frost, G. J., Lee, S.-H., Trainer, M., Richter, A., Angevine, W. M., Atlas, E., Bianco, L., Boersma, K. F., Brioude, J., Burrows, J. P., De Gouw, J., Fried, A., Gleason, J., Hilboll, A., Mellqvist, J., Peischl, J., Richter, D., Rivera, C., Ryerson, T., Te Lintel Hekkert, S., Walega, J., Warneke, C., Weibring, P., and Williams, E.: Evaluations of NOx and highly reactive VOC emission inventories in Texas and their implications for ozone plume simulations during the Texas Air Quality
830   Study 2006, Atmospheric Chem. Phys., 11, 11361–11386, https://doi.org/10.5194/acp-11-11361-2011, 2011.

Kleinman, L. I.: The dependence of tropospheric ozone production rate on ozone precursors, Atmos. Environ., 39, 575–586, https://doi.org/10.1016/j.atmosenv.2004.08.047, 2005.

Kleinman, L. I., Daum, P. H., Lee, Y.-N., Nunnermacker, L. J., Springston, S. R., Weinstein-Lloyd, J., and Rudolph, J.: Sensitivity of ozone production rate to ozone precursors, Geophys. Res. Lett., 28, 2903–2906,
835   https://doi.org/10.1029/2000GL012597, 2001.

Lebo, Z. J. and Morrison, H.: Effects of Horizontal and Vertical Grid Spacing on Mixing in Simulated Squall Lines and Implications for Convective Strength and Structure, Mon. Weather Rev., 143, 4355–4375, https://doi.org/10.1175/MWR-D-15-0154.1, 2015.

Leong, Y. J., Sanchez, N. P., Wallace, H. W., Karakurt Cevik, B., Hernandez, C. S., Han, Y., Flynn, J. H., Massoli, P.,
840 Floerchinger, C., Fortner, E. C., Herndon, S., Bean, J. K., Hildebrandt Ruiz, L., Jeon, W., Choi, Y., Lefer, B., and Griffin, R.
J.: Overview of surface measurements and spatial characterization of submicrometer particulate matter during the DISCOVER-
AQ 2013 campaign in Houston, TX, J. Air Waste Manag. Assoc., 67, 854–872,
https://doi.org/10.1080/10962247.2017.1296502, 2017.

Li, J., An, X., Cui, M., Sun, Z., Wang, C., and Li, Y.: Simulation study on regional atmospheric oxidation capacity and
845 precursor sensitivity, Atmos. Environ., 263, 118657, https://doi.org/10.1016/j.atmosenv.2021.118657, 2021.

Li, L., Chen, C., Huang, C., Huang, H., Zhang, G., Wang, Y., Chen, M., Wang, H., Chen, Y., Streets, D. G., and Fu, J.: Ozone
sensitivity analysis with the MM5-CMAQ modeling system for Shanghai, J. Environ. Sci., 23, 1150–1157,
https://doi.org/10.1016/S1001-0742(10)60527-X, 2011.

Li, W., Wang, Y., Flynn, J., Griffin, R. J., Guo, F., and Schnell, J. L.: Spatial Variation of Surface O3 Responses to Drought
850 Over the Contiguous United States During Summertime: Role of Precursor Emissions and Ozone Chemistry, J. Geophys. Res.
Atmospheres, 127, e2021JD035607, https://doi.org/10.1029/2021JD035607, 2022.

Li, W., Wang, Y., Liu, X., Soleimanian, E., Griggs, T., Flynn, J., and Walter, P.: Understanding offshore high-ozone events
during TRACER-AQ 2021 in Houston: insights from WRF–CAMx photochemical modeling, Atmospheric Chem. Phys., 23,
13685–13699, https://doi.org/10.5194/acp-23-13685-2023, 2023.

855 Li, Y., Barth, M. C., Chen, G., Patton, E. G., Kim, S.-W., Wisthaler, A., Mikoviny, T., Fried, A., Clark, R., and Steiner, A. L.:
Large-eddy simulation of biogenic VOC chemistry during the DISCOVER-AQ 2011 campaign, J. Geophys. Res.
Atmospheres, 121, 8083–8105, https://doi.org/10.1002/2016JD024942, 2016.

Li, Z., Xue, L., Yang, X., Zha, Q., Tham, Y. J., Yan, C., Louie, P. K. K., Luk, C. W. Y., Wang, T., and Wang, W.: Oxidizing
capacity of the rural atmosphere in Hong Kong, Southern China, Sci. Total Environ., 612, 1114–1122,
860 https://doi.org/10.1016/j.scitotenv.2017.08.310, 2018.

Liang, Z., Rao, J., Guo, D., and Lu, Q.: Simulation and projection of the sudden stratospheric warming events in different
scenarios by CESM2-WACCM, Clim. Dyn., 59, 3741–3761, https://doi.org/10.1007/s00382-022-06293-2, 2022.

Liu, T., Mickley, L. J., Marlier, M. E., DeFries, R. S., Khan, M. F., Latif, M. T., and Karambelas, A.: Diagnosing spatial biases
and uncertainties in global fire emissions inventories: Indonesia as regional case study, Remote Sens. Environ., 237, 111557,
865 https://doi.org/10.1016/j.rse.2019.111557, 2020.

Liu, T., Hong, Y., Li, M., Xu, L., Chen, J., Bian, Y., Yang, C., Dan, Y., Zhang, Y., Xue, L., Zhao, M., Huang, Z., and Wang,
H.: Atmospheric oxidation capacity and ozone pollution mechanism in a coastal city of southeastern China: analysis of a
typical photochemical episode by an observation-based model, Atmospheric Chem. Phys., 22, 2173–2190,
https://doi.org/10.5194/acp-22-2173-2022, 2022.

870 Liu, X., Wang, Y., Wasti, S., Li, W., Soleimanian, E., Flynn, J., Griggs, T., Alvarez, S., Sullivan, J. T., Roots, M., Twigg, L.,
Gronoff, G., Berkoff, T., Walter, P., Estes, M., Hair, J. W., Shingler, T., Scarino, A. J., Fenn, M., and Judd, L.: Evaluating

WRF-GC v2.0 predictions of boundary layer height and vertical ozone profile during the 2021 TRACER-AQ campaign in Houston, Texas, Geosci. Model Dev., 16, 5493–5514, https://doi.org/10.5194/gmd-16-5493-2023, 2023.

Ma, X., Tan, Z., Lu, K., Yang, X., Chen, X., Wang, H., Chen, S., Fang, X., Li, S., Li, X., Liu, J., Liu, Y., Lou, S., Qiu, W., Wang, H., Zeng, L., and Zhang, Y.: OH and HO$_2$ radical chemistry at a suburban site during the EXPLORE-YRD campaign in 2018, Atmospheric Chem. Phys., 22, 7005–7028, https://doi.org/10.5194/acp-22-7005-2022, 2022.

Mao, J., Ren, X., Chen, S., Brune, W. H., Chen, Z., Martinez, M., Harder, H., Lefer, B., Rappenglück, B., Flynn, J., and Leuchner, M.: Atmospheric oxidation capacity in the summer of Houston 2006: Comparison with summer measurements in other metropolitan studies, Atmos. Environ., 44, 4107–4115, https://doi.org/10.1016/j.atmosenv.2009.01.013, 2010.

Marsha, A., Sain, S. R., Heaton, M. J., Monaghan, A. J., and Wilhelmi, O. V.: Influences of climatic and population changes on heat-related mortality in Houston, Texas, USA, Clim. Change, 146, 471–485, https://doi.org/10.1007/s10584-016-1775-1, 2018.

Martins, D. K., Najjar, R. G., Tzortziou, M., Abuhassan, N., Thompson, A. M., and Kollonige, D. E.: Spatial and temporal variability of ground and satellite column measurements of NO2 and O3 over the Atlantic Ocean during the Deposition of Atmospheric Nitrogen to Coastal Ecosystems Experiment, J. Geophys. Res. Atmospheres, 121, 14,175-14,187, https://doi.org/10.1002/2016JD024998, 2016.

Mazzuca, G. M., Ren, X., Loughner, C. P., Estes, M., Crawford, J. H., Pickering, K. E., Weinheimer, A. J., and Dickerson, R. R.: Ozone production and its sensitivity to NO$_x$ and VOCs: results from the DISCOVER-AQ field experiment, Houston 2013, Atmospheric Chem. Phys., 16, 14463–14474, https://doi.org/10.5194/acp-16-14463-2016, 2016.

Miao, Y., Li, J., Miao, S., Che, H., Wang, Y., Zhang, X., Zhu, R., and Liu, S.: Interaction Between Planetary Boundary Layer and PM2.5 Pollution in Megacities in China: a Review, Curr. Pollut. Rep., 5, 261–271, https://doi.org/10.1007/s40726-019-00124-5, 2019.

Morgenstern, O., Zeng, G., Luke Abraham, N., Telford, P. J., Braesicke, P., Pyle, J. A., Hardiman, S. C., O'Connor, F. M., and Johnson, C. E.: Impacts of climate change, ozone recovery, and increasing methane on surface ozone and the tropospheric oxidizing capacity, JGR Atmospheres, 118, 1028–1041, https://doi.org/10.1029/2012JD018382, 2013.

Morris, G. A., Hersey, S., Thompson, A. M., Pawson, S., Nielsen, J. E., Colarco, P. R., McMillan, W. W., Stohl, A., Turquety, S., Warner, J., Johnson, B. J., Kucsera, T. L., Larko, D. E., Oltmans, S. J., and Witte, J. C.: Alaskan and Canadian forest fires exacerbate ozone pollution over Houston, Texas, on 19 and 20 July 2004, J. Geophys. Res. Atmospheres, 111, https://doi.org/10.1029/2006JD007090, 2006.

Morrison, H., Thompson, G., and Tatarskii, V.: Impact of Cloud Microphysics on the Development of Trailing Stratiform Precipitation in a Simulated Squall Line: Comparison of One- and Two-Moment Schemes, Mon. Weather Rev., 137, 991–1007, https://doi.org/10.1175/2008MWR2556.1, 2009.

Murphy, C. F. and Allen, D. T.: Hydrocarbon emissions from industrial release events in the Houston-Galveston area and their impact on ozone formation, Atmos. Environ., 39, 3785–3798, https://doi.org/10.1016/j.atmosenv.2005.02.051, 2005.

905 Nam, J., Kimura, Y., Vizuete, W., Murphy, C., and Allen, D. T.: Modeling the impacts of emission events on ozone formation in Houston, Texas, Atmos. Environ., 40, 5329–5341, https://doi.org/10.1016/j.atmosenv.2006.05.002, 2006.

NCEP: NCEP FNL Operational Model Global Tropospheric Analyses, continuing from July 1999. Research Data Archive at the National Center for Atmospheric Research, Computational and Information Systems Laboratory., 2000.

Nowlan, C. R., Liu, X., Janz, S. J., Kowalewski, M. G., Chance, K., Follette-Cook, M. B., Fried, A., González Abad, G.,

910 Herman, J. R., Judd, L. M., Kwon, H.-A., Loughner, C. P., Pickering, K. E., Richter, D., Spinei, E., Walega, J., Weibring, P., and Weinheimer, A. J.: Nitrogen dioxide and formaldehyde measurements from the GEOstationary Coastal and Air Pollution Events (GEO-CAPE) Airborne Simulator over Houston, Texas, Atmospheric Meas. Tech., 11, 5941–5964, https://doi.org/10.5194/amt-11-5941-2018, 2018.

Nussbaumer, C. M., Crowley, J. N., Schuladen, J., Williams, J., Hafermann, S., Reiffs, A., Axinte, R., Harder, H., Ernest, C.,

915 Novelli, A., Sala, K., Martinez, M., Mallik, C., Tomsche, L., Plass-Dülmer, C., Bohn, B., Lelieveld, J., and Fischer, H.: Measurement report: Photochemical production and loss rates of formaldehyde and ozone across Europe, Atmospheric Chemistry and Physics, 21, 18413–18432, https://doi.org/10.5194/acp-21-18413-2021, 2021.

Ochsner, T. E., Cosh, M. H., Cuenca, R. H., Dorigo, W. A., Draper, C. S., Hagimoto, Y., Kerr, Y. H., Larson, K. M., Njoku, E. G., Small, E. E., and Zreda, M.: State of the Art in Large-Scale Soil Moisture Monitoring, Soil Science Society of

920 America Journal, 77, 1888–1919, https://doi.org/10.2136/sssaj2013.03.0093, 2013.
Parrish, D. D., Allen, D. T., Bates, T. S., Estes, M., Fehsenfeld, F. C., Feingold, G., Ferrare, R., Hardesty, R. M., Meagher, J. F., Nielsen-Gammon, J. W., Pierce, R. B., Ryerson, T. B., Seinfeld, J. H., and Williams, E. J.: Overview of the Second Texas Air Quality Study (TexAQS II) and the Gulf of Mexico Atmospheric Composition and Climate Study (GoMACCS), J. Geophys. Res. Atmospheres, 114, https://doi.org/10.1029/2009JD011842, 2009.

925 Parrish, D. D., Ryerson, T. B., Mellqvist, J., Johansson, J., Fried, A., Richter, D., Walega, J. G., Washenfelder, R. A., de Gouw, J. A., Peischl, J., Aikin, K. C., McKeen, S. A., Frost, G. J., Fehsenfeld, F. C., and Herndon, S. C.: Primary and secondary sources of formaldehyde in urban atmospheres: Houston Texas region, Atmospheric Chem. Phys., 12, 3273–3288, https://doi.org/10.5194/acp-12-3273-2012, 2012.

Perring, A. E., Pusede, S. E., and Cohen, R. C.: An Observational Perspective on the Atmospheric Impacts of Alkyl and

930 Multifunctional Nitrates on Ozone and Secondary Organic Aerosol, Chem. Rev., 113, 5848–5870, https://doi.org/10.1021/cr300520x, 2013.

Pinto, J. O., Jensen, A. A., Jiménez, P. A., Hertneky, T., Muñoz-Esparza, D., Dumont, A., and Steiner, M.: Real-time WRF large-eddy simulations to support uncrewed aircraft system (UAS) flight planning and operations during 2018 LAPSE-RATE, Earth Syst. Sci. Data, 13, 697–711, https://doi.org/10.5194/essd-13-697-2021, 2021.

935 Platt, U. and Stutz, J.: Differential Absorption Spectroscopy, in: Differential Optical Absorption Spectroscopy, Springer Berlin Heidelberg, Berlin, Heidelberg, 135–174, https://doi.org/10.1007/978-3-540-75776-4_6, 2008.
Rammah, A., Whitworth, K. W., and Symanski, E.: Particle air pollution and gestational diabetes mellitus in Houston, Texas, Environ. Res., 190, https://doi.org/10.1016/j.envres.2020.109988, 2020.

Ren, X., van Duin, D., Cazorla, M., Chen, S., Mao, J., Zhang, L., Brune, W. H., Flynn, J. H., Grossberg, N., Lefer, B. L.,
940   Rappenglück, B., Wong, K. W., Tsai, C., Stutz, J., Dibb, J. E., Thomas Jobson, B., Luke, W. T., and Kelley, P.: Atmospheric
oxidation chemistry and ozone production: Results from SHARP 2009 in Houston, Texas, J. Geophys. Res. Atmospheres, 118,
5770–5780, https://doi.org/10.1002/jgrd.50342, 2013.

Rinne, H. J. I., Guenther, A. B., Greenberg, J. P., and Harley, P. C.: Isoprene and monoterpene fluxes measured above
Amazonian rainforest and their dependence on light and temperature, Atmos. Environ., 36, 2421–2426,
945   https://doi.org/10.1016/S1352-2310(01)00523-4, 2002.

Sadeghi, B., Pouyaei, A., Choi, Y., and Rappenglueck, B.: Influence of seasonal variability on source characteristics of VOCs
at Houston industrial area, Atmos. Environ., 277, https://doi.org/10.1016/j.atmosenv.2022.119077, 2022.

Schade, G. W. and Roest, G.: Source apportionment of non-methane hydrocarbons, NOx and H2S data from a central
monitoring station in the Eagle Ford shale, Texas, Elem. Sci. Anthr., 6, 35, https://doi.org/10.1525/elementa.289, 2018.

950   Schroeder, J. R., Crawford, J. H., Fried, A., Walega, J., Weinheimer, A., Wisthaler, A., Müller, M., Mikoviny, T., Chen, G.,
Shook, M., Blake, D. R., and Tonnesen, G. S.: New insights into the column CH2O/NO2 ratio as an indicator of near-surface
ozone sensitivity, J. Geophys. Res. Atmospheres, 122, 8885–8907, https://doi.org/10.1002/2017JD026781, 2017.

Shahriar, Md. T., Kadiyala, A., Kommalapati, R., and Huque, Z.: A Review of Ozone Studies in the
Houston−Galveston−Brazoria Nonattainment Area, in: Trace Materials in Air, Soil, and Water, vol. 1210, American Chemical
955   Society, 37–50, https://doi.org/10.1021/bk-2015-1210.ch002, 2015.

Shrestha, S., Yoon, S., Alvarez, S. L., Wang, Y., Flynn, J. H., Usenko, S., and Sheesley, R. J.: Emission Ratios and Diurnal
Variability of Volatile Organic Compounds and Influence of Industrial Emissions in Two Texas Cities, Atmosphere, 14, 1006,
https://doi.org/10.3390/atmos14061006, 2023.

Sillman, S., Vautard, R., Menut, L., and Kley, D.: O3-NOx-VOC sensitivity and NOx-VOC indicators in Paris: Results from
960   models and Atmospheric Pollution Over the Paris Area (ESQUIF) measurements, J. Geophys. Res. Atmospheres, 108,
https://doi.org/10.1029/2002JD001561, 2003.

Silvern, R. F., Jacob, D. J., Mickley, L. J., Sulprizio, M. P., Travis, K. R., Marais, E. A., Cohen, R. C., Laughner, J. L., Choi,
S., Joiner, J., and Lamsal, L. N.: Using satellite observations of tropospheric NO$_2$ columns to infer long-term trends in US NO$_x$
emissions: the importance of accounting for the free tropospheric NO$_2$ background, Atmospheric Chem. Phys., 19, 8863–8878,
965   https://doi.org/10.5194/acp-19-8863-2019, 2019.

Soleimanian, E., Wang, Y., Li, W., Liu, X., Griggs, T., Flynn, J., Walter, P. J., and Estes, M. J.: Understanding ozone episodes
during the TRACER-AQ campaign in Houston, Texas: The role of transport and ozone production sensitivity to precursors,
Sci. Total Environ., 900, 165881, https://doi.org/10.1016/j.scitotenv.2023.165881, 2023.

Song, J., Lei, W., Bei, N., Zavala, M., de Foy, B., Volkamer, R., Cardenas, B., Zheng, J., Zhang, R., and Molina, L. T.: Ozone
970   response to emission changes: a modeling study during the MCMA-2006/MILAGRO Campaign, Atmospheric Chem. Phys.,
10, 3827–3846, https://doi.org/10.5194/acp-10-3827-2010, 2010.

Souri, A. H., Choi, Y., Li, X., Kotsakis, A., and Jiang, X.: A 15-year climatology of wind pattern impacts on surface ozone in Houston, Texas, Atmospheric Res., 174–175, 124–134, https://doi.org/10.1016/j.atmosres.2016.02.007, 2016a.

Souri, A. H., Choi, Y., Jeon, W., Li, X., Pan, S., Diao, L., and Westenbarger, D. A.: Constraining NOx emissions using satellite NO2 measurements during 2013 DISCOVER-AQ Texas campaign, Atmos. Environ., 131, 371–381, https://doi.org/10.1016/j.atmosenv.2016.02.020, 2016b.

Souri, A. H., Choi, Y., Pan, S., Curci, G., Nowlan, C. R., Janz, S. J., Kowalewski, M. G., Liu, J., Herman, J. R., and Weinheimer, A. J.: First Top-Down Estimates of Anthropogenic NOx Emissions Using High-Resolution Airborne Remote Sensing Observations, J. Geophys. Res. Atmospheres, 123, 3269–3284, https://doi.org/10.1002/2017JD028009, 2018.

Souri, A. H., Nowlan, C. R., Wolfe, G. M., Lamsal, L. N., Chan Miller, C. E., Abad, G. G., Janz, S. J., Fried, A., Blake, D. R., Weinheimer, A. J., Diskin, G. S., Liu, X., and Chance, K.: Revisiting the effectiveness of HCHO/NO2 ratios for inferring ozone sensitivity to its precursors using high resolution airborne remote sensing observations in a high ozone episode during the KORUS-AQ campaign, Atmos. Environ., 224, 117341, https://doi.org/10.1016/j.atmosenv.2020.117341, 2020.

Spinei, E., Whitehill, A., Fried, A., Tiefengraber, M., Knepp, T. N., Herndon, S., Herman, J. R., Müller, M., Abuhassan, N., Cede, A., Richter, D., Walega, J., Crawford, J., Szykman, J., Valin, L., Williams, D. J., Long, R., Swap, R. J., Lee, Y., Nowak, N., and Poche, B.: The first evaluation of formaldehyde column observations by improved Pandora spectrometers during the KORUS-AQ field study, Atmospheric Meas. Tech., 11, 4943–4961, https://doi.org/10.5194/amt-11-4943-2018, 2018.

Spiridonov, V., Jakimovski, B., Spiridonova, I., and Pereira, G.: Development of air quality forecasting system in Macedonia, based on WRF-Chem model, Air Qual. Atmosphere Health, 12, 825–836, https://doi.org/10.1007/s11869-019-00698-5, 2019.

Sprengnether, M., Demerjian, K. L., Donahue, N. M., and Anderson, J. G.: Product analysis of the OH oxidation of isoprene and 1,3-butadiene in the presence of NO, J. Geophys. Res. Atmospheres, 107, ACH 8-1-ACH 8-13, https://doi.org/10.1029/2001JD000716, 2002.

Stockwell, W. R.: Effects of turbulence on gas-phase atmospheric chemistry: Calculation of the relationship between time scales for diffusion and chemical reaction, Meteorol. Atmospheric Phys., 57, 159–171, https://doi.org/10.1007/BF01044159, 1995.

Tan, Z., Lu, K., Jiang, M., Su, R., Wang, H., Lou, S., Fu, Q., Zhai, C., Tan, Q., Yue, D., Chen, D., Wang, Z., Xie, S., Zeng, L., and Zhang, Y.: Daytime atmospheric oxidation capacity in four Chinese megacities during the photochemically polluted season: a case study based on box model simulation, Atmospheric Chem. Phys., 19, 3493–3513, https://doi.org/10.5194/acp-19-3493-2019, 2019.

Tang, G., Wang, Y., Li, X., Ji, D., Hsu, S., and Gao, X.: Spatial-temporal variations in surface ozone in Northern China as observed during 2009–2010 and possible implications for future air quality control strategies, Atmospheric Chem. Phys., 12, 2757–2776, https://doi.org/10.5194/acp-12-2757-2012, 2012.

Tang, W., Pfister, G. G., Kumar, R., Barth, M., Edwards, D. P., Emmons, L. K., and Tilmes, S.: Capturing High-Resolution Air Pollution Features Using the Multi-Scale Infrastructure for Chemistry and Aerosols Version 0 (MUSICAv0) Global Modeling System, JGR Atmospheres, 128, e2022JD038345, https://doi.org/10.1029/2022JD038345, 2023.

Thompson, A. M., Stauffer, R. M., Boyle, T. P., Kollonige, D. E., Miyazaki, K., Tzortziou, M., Herman, J. R., Abuhassan, N., Jordan, C. E., and Lamb, B. T.: Comparison of Near-Surface NO2 Pollution With Pandora Total Column NO2 During the Korea-United States Ocean Color (KORUS OC) Campaign, J. Geophys. Res. Atmospheres, 124, 13560–13575, https://doi.org/10.1029/2019JD030765, 2019.

1010 Tie, X., Madronich, S., Walters, S., Zhang, R., Rasch, P., and Collins, W.: Effect of clouds on photolysis and oxidants in the troposphere, J. Geophys. Res. Atmospheres, 108, https://doi.org/10.1029/2003JD003659, 2003.

Tonnesen, G. S. and Dennis, R. L.: Analysis of radical propagation efficiency to assess ozone sensitivity to hydrocarbons and NO x : 2. Long-lived species as indicators of ozone concentration sensitivity, J. Geophys. Res. Atmospheres, 105, 9227–9241, https://doi.org/10.1029/1999JD900372, 2000.

1015 Uebel, M. and Bott, A.: Influence of complex terrain and anthropogenic emissions on atmospheric CO2 patterns–a high-resolution numerical analysis, Q. J. R. Meteorol. Soc., 144, 34–47, https://doi.org/10.1002/qj.3182, 2018.

Vizuete, W., Nielsen-Gammon, J., Dickey, J., Couzo, E., Blanchard, C., Breitenbach, P., Rasool, Q. Z., and Byun, D.: Meteorological based parameters and ozone exceedances in Houston and other cities in Texas, J. Air Waste Manag. Assoc., 72, 969–984, https://doi.org/10.1080/10962247.2022.2064004, 2022.

1020 Wang, S., Coggon, M. M., Gkatzelis, G. I., Warneke, C., Bourgeois, I., Ryerson, T., Peischl, J., Veres, P. R., Neuman, J. A., Hair, J., Shingler, T., Fenn, M., Diskin, G., Huey, L. G., Lee, Y. R., Apel, E. C., Hornbrook, R. S., Hills, A. J., Hall, S. R., Ullmann, K., Bela, M. M., Trainer, M. K., Kumar, R., Orlando, J. J., Flocke, F. M., and Emmons, L. K.: Chemical Tomography in a Fresh Wildland Fire Plume: A Large Eddy Simulation (LES) Study, J. Geophys. Res. Atmospheres, 126, e2021JD035203, https://doi.org/10.1029/2021JD035203, 2021.

1025 Ward, N. D., Megonigal, J. P., Bond-Lamberty, B., Bailey, V. L., Butman, D., Canuel, E. A., Diefenderfer, H., Ganju, N. K., Goñi, M. A., Graham, E. B., Hopkinson, C. S., Khangaonkar, T., Langley, J. A., McDowell, N. G., Myers-Pigg, A. N., Neumann, R. B., Osburn, C. L., Price, R. M., Rowland, J., Sengupta, A., Simard, M., Thornton, P. E., Tzortziou, M., Vargas, R., Weisenhorn, P. B., and Windham-Myers, L.: Representing the function and sensitivity of coastal interfaces in Earth system models, Nat Commun, 11, 2458, https://doi.org/10.1038/s41467-020-16236-2, 2020.

1030 Wang, Y., Ma, Y.-F., Muñoz-Esparza, D., Dai, J., Li, C. W. Y., Lichtig, P., Tsang, R. C. W., Liu, C.-H., Wang, T., and Brasseur, G. P.: Coupled mesoscale-LES modeling of air quality in a polluted city using WRF-LES-Chem, Atmospheric Chem. Phys., 23, 5905-5927, https://doi.org/10.5194/acp-23-5905-2023, 2023.

Whalley, L. K., Stone, D., Bandy, B., Dunmore, R., Hamilton, J. F., Hopkins, J., Lee, J. D., Lewis, A. C., and Heard, D. E.: Atmospheric OH reactivity in central London: observations, model predictions and estimates of in situ ozone production,
1035 Atmospheric Chem. Phys., 16, 2109–2122, https://doi.org/10.5194/acp-16-2109-2016, 2016.

Wiedinmyer, C., Kimura, Y., McDonald-Buller, E. C., Emmons, L. K., Buchholz, R. R., Tang, W., Seto, K., Joseph, M. B., Barsanti, K. C., Carlton, A. G., and Yokelson, R.: The Fire Inventory from NCAR version 2.5: an updated global fire emissions model for climate and chemistry applications, Atmospheric sciences, https://doi.org/10.5194/egusphere-2023-124, 2023.

Wong, K. W., Tsai, C., Lefer, B., Grossberg, N., and Stutz, J.: Modeling of daytime HONO vertical gradients during SHARP
1040 2009, Atmospheric Chem. Phys., 13, 3587–3601, https://doi.org/10.5194/acp-13-3587-2013, 2013.

Xiang, Y., Zhang, T., Liu, J., Lv, L., Dong, Y., and Chen, Z.: Atmosphere boundary layer height and its effect on air pollutants in Beijing during winter heavy pollution, Atmospheric Res., 215, 305–316, https://doi.org/10.1016/j.atmosres.2018.09.014, 2019.

Xue, L., Gu, R., Wang, T., Wang, X., Saunders, S., Blake, D., Louie, P. K. K., Luk, C. W. Y., Simpson, I., Xu, Z., Wang, Z., Gao, Y., Lee, S., Mellouki, A., and Wang, W.: Oxidative capacity and radical chemistry in the polluted atmosphere of Hong Kong and Pearl River Delta region: analysis of a severe photochemical smog episode, Atmospheric Chem. Phys., 16, 9891–9903, https://doi.org/10.5194/acp-16-9891-2016, 2016.

Yang, Y., Shao, M., Wang, X., Nölscher, A. C., Kessel, S., Guenther, A., and Williams, J.: Towards a quantitative understanding of total OH reactivity: A review, Atmos. Environ., 134, 147–161, https://doi.org/10.1016/j.atmosenv.2016.03.010, 2016.

Ye, L., Wang, X., Fan, S., Chen, W., Chang, M., Zhou, S., Wu, Z., and Fan, Q.: Photochemical indicators of ozone sensitivity: application in the Pearl River Delta, China, Front. Environ. Sci. Eng., 10, 15, https://doi.org/10.1007/s11783-016-0887-1, 2016.

Yu, D., Tan, Z., Lu, K., Ma, X., Li, X., Chen, S., Zhu, B., Lin, L., Li, Y., Qiu, P., Yang, X., Liu, Y., Wang, H., He, L., Huang, X., and Zhang, Y.: An explicit study of local ozone budget and NOx-VOCs sensitivity in Shenzhen China, Atmos. Environ., 224, 117304, https://doi.org/10.1016/j.atmosenv.2020.117304, 2020.

Zeng, J., Zhang, Y., Mu, Z., Pang, W., Zhang, H., Wu, Z., Song, W., and Wang, X.: Temperature and light dependency of isoprene and monoterpene emissions from tropical and subtropical trees: Field observations in south China, Appl. Geochem., 155, 105727, https://doi.org/10.1016/j.apgeochem.2023.105727, 2023.

Zhang, G., Sun, Y., Xu, W., Wu, L., Duan, Y., Liang, L., and Li, Y.: Identifying the O3 chemical regime inferred from the weekly pattern of atmospheric O3, CO, NOx, and PM10: Five-year observations at a center urban site in Shanghai, China, Sci. Total Environ., 888, 164079, https://doi.org/10.1016/j.scitotenv.2023.164079, 2023.

Zhang, H., Zheng, Z., Yu, T., Liu, C., Qian, H., and Li, J.: Seasonal and diurnal patterns of outdoor formaldehyde and impacts on indoor environments and health, Environ. Res., 205, 112550, https://doi.org/10.1016/j.envres.2021.112550, 2022.

Zhou, W., Cohan, D. S., and Henderson, B. H.: Slower ozone production in Houston, Texas following emission reductions: Evidence from Texas Air Quality Studies in 2000 and 2006, Atmospheric Chem. Phys., 14, 2777–2788, https://doi.org/10.5194/acp-14-2777-2014, 2014.

Zhu, J., Wang, S., Wang, H., Jing, S., Lou, S., Saiz-Lopez, A., and Zhou, B.: Observationally constrained modeling of atmospheric oxidation capacity and photochemical reactivity in Shanghai, China, Atmospheric Chem. Phys., 20, 1217–1232, https://doi.org/10.5194/acp-20-1217-2020, 2020.